J4929SU

PNL-8042
UC-313

Inert Electrodes Program

# Final Report on the Application of Chaos Theory to an Alumina Sensor for Aluminum Reduction Cells

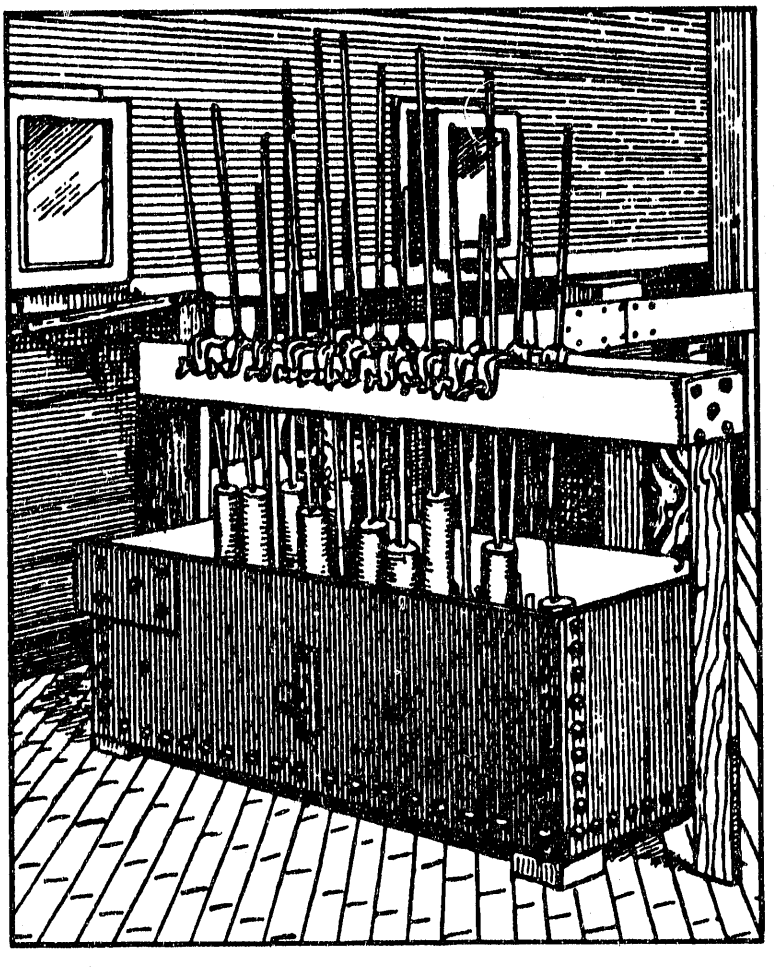

March 1992

Work Supported by the U.S. Department of Energy
under Contract DE-AC06-76RLO 1830

Pacific Northwest Laboratory
Operated for the U.S. Department of Energy
by Battelle Memorial Institute

Battelle

DISTRIBUTION OF THIS DOCUMENT IS UNLIMITED

PNL-8042

## DISCLAIMER

This report was prepared as an account of work sponsored by an agency of the United States Government. Neither the United States Government nor any agency thereof, nor Battelle Memorial Institute, nor any of their employees, makes **any warranty, expressed or implied, or assumes any legal liability or responsibility for the accuracy, completeness, or usefulness of any information, apparatus, product, or process disclosed, or represents that its use would not infringe privately owned rights.** Reference herein to any specific commercial product, process, or service by trade name, trademark, manufacturer, or otherwise does not necessarily constitute or imply its endorsement, recommendation, or favoring by the United States Government or any agency thereof, or Battelle Memorial Institute. The views and opinions of authors expressed herein do not necessarily state or reflect those of the United States Government or any agency thereof.

PACIFIC NORTHWEST LABORATORY
*operated by*
BATTELLE MEMORIAL INSTITUTE
*for the*
UNITED STATES DEPARTMENT OF ENERGY
*under Contract DE-AC06-76RLO 1830*

**Printed in the United States of America**

**Available to DOE and DOE contractors from the Office of Scientific and Technical Information, P.O. Box 62, Oak Ridge, TN 37831; prices available from (615) 576-8401. FTS 626-8401.**

**Available to the public from the National Technical Information Service, U.S. Department of Commerce, 5285 Port Royal Rd., Springfield, VA 22161.**

PNL--8042

DE92 010630

Inert Electrodes Program

# FINAL REPORT ON THE APPLICATION OF CHAOS THEORY TO AN ALUMINA SENSOR FOR ALUMINUM REDUCTION CELLS

R. E. Williford
C. F. Windisch, Jr., Program Manager

March 1992

Prepared for the
U.S. Department of Energy
under Contract DE-AC06-76RLO 1830

Pacific Northwest Laboratory
Richland, Washington 99352

MASTER

# PREFACE

The Office of Industrial Processes (OIP) of the Department of Energy (DOE) has supported research at the Pacific Northwest Laboratory (PNL) since FY 1986 to develop sensors for aluminum electrolysis cells in conjunction with efforts to develop and test cermet inert anodes. Based on discussions with DOE/OIP, the scope of the Sensors Development Program was narrowed in FY 1990 to the development of an alumina sensor. Specifically, various digital signal analysis (DSA) methods were to be evaluated as the possible basis for measuring alumina concentrations. This approach has the advantage that the data are collected from existing components of the electrolysis cell. Consequently, no new probes or materials have to be inserted into the molten electrolyte and, therefore, evaluated for chemical compatibility or corrosion resistance.

This report summarizes the results of one type of DSA study. In this study, DSA approaches based on "chaos theory" were applied to data collected from two types of experiments: 1) bench-scale laboratory tests, and 2) a full-scale pilot cell test. The objectives were to determine if any of the computed analysis parameters exhibited sensitivity to the alumina concentration and if that sensitivity showed consistent trends with concentration and time. In this way, the results could be used to assess the feasibility of an alumina sensor based on chaos theory. This study was initiated in January 1990. Another set of DSA analyses are being performed using more classical methods and was discussed in a separate PNL document (Windisch et al. 1990).

## SUMMARY

Four chaos-related digital signal analysis (DSA) methods were applied to the analysis of voltage and current signals collected from aluminum electrolysis cells. Two separate data bases were analyzed: bench-scale laboratory experiments and a pilot-scale test. The objective was to assess the feasibility of using these types of data and analysis methods as the basis for a non-intrusive sensor to measure the alumina content in the electrolysis bath. This was the first time chaos theory approaches have been employed to analyze aluminum electrolysis cells.

In the first approach, phase space plots were developed from the data bases. Results for the laboratory experiments were inconclusive because no distinct patterns were found in the plots. Although the pilot cell test data exhibited distinct and recognizable patterns, there was no apparent correlation with the alumina concentration in the electrolyte bath. Adequate sensitivity was exhibited, but consistency was insufficient, and the approach was thus not successful.

The second approach employed the Hurst exponent analysis, which gave obvious results for the laboratory tests, and simply detected the rectifier period in the pilot cell test data.

The third and fourth approaches concerned multifractal analyses based on thermodynamic and probabilistic arguments, respectively. The thermodynamic approach was applied only to the laboratory data, and showed adequate sensitivity and encouraging consistency, despite the lack of computational accuracy. An order of magnitude increase in computational accuracy was obtained from the probabilistic multifractal approach, which showed that the lack of reliable consistency in the results had originated from the scatter in the laboratory data itself. It was thought that an improved method of data collection during the pilot cell test would provide the desired consistency, but this was not the case. It appears that the physical phenomena occurring in the pilot cell test were much too complex to be detected adequately by the

measurement of the current and/or voltage from just one of six inert electrodes. Recommendations for future work are provided at the end of this report.

## ACKNOWLEDGMENTS

The authors would like to acknowledge the assistance of N. D. Stice and N. C. Davis in the laboratory tests, and the cooperation of the Reynolds Metals Company research staff in performing the pilot cell test at the Reynolds Manufacturing Technology Laboratory in Sheffield, AL. The assistance of PNL staff in collecting the chaos theory data during the pilot cell test is also acknowledged, especially E. N. Greenwell who helped design the instrumental setup for data acquisition. The authors are also grateful for the programmatic support by M. J. McMonigle and the Office of Industrial Processes of the U.S. Department of Energy.

CONTENTS

PREFACE . . . . . iii

SUMMARY . . . . . v

ACKNOWLEDGMENTS . . . . . vii

1.0 INTRODUCTION . . . . . 1.1

2.0 EXPERIMENTAL PROCEDURES . . . . . 2.1

2.1 LABORATORY EXPERIMENTS . . . . . 2.1

2.2 PILOT CELL TEST . . . . . 2.3

3.0 DATA ANALYSIS USING CHAOS THEORY . . . . . 3.1

3.1 PHASE SPACE PLOTS . . . . . 3.1

3.1.1 Results for Laboratory Experiments . . . . . 3.2

3.1.2 Results for Pilot Cell Test . . . . . 3.2

3.2 HURST EXPONENTS . . . . . 3.5

3.2.1 Results for Laboratory Tests . . . . . 3.5

3.2.2 Results for Pilot Cell Test . . . . . 3.8

3.3 MULTIFRACTALS . . . . . 3.8

3.3.1 Thermodynamic Formalism . . . . . 3.11

3.3.2 Probabilistic Formalism . . . . . 3.17

3.4 OTHER APPROACHES . . . . . 3.30

4.0 FEASIBILITY ASSESSMENT . . . . . 4.1

5.0 CONCLUSIONS AND RECOMMENDATIONS . . . . . 5.1

6.0 REFERENCES . . . . . 6.1

## FIGURES


2.1 Apparatus for Collecting Digital Signals from Bench-Scale Aluminum Electrolysis Cells . . . . . 2.2

2.2 Top View of Pilot Cell Anodes Showing Relative Anode Positions . . . . . 2.5

2.3a Block Diagrams of Signal Acquisition System for Pilot Cell Test . . . . . 2.7

2.3b Block Diagrams of Signal Acquisition System for Pilot Cell Test . . . . . 2.8

2.4 Alumina Concentration Versus Time for the Pilot Cell Test . . 2.14

3.1 Phase Space Plot for File RW3A of the Pilot Cell Test, 85% Alumina . . . . . 3.3

3.2 Phase Space Plot for File RW1A of the Pilot Cell Test, 76% Alumina . . . . . 3.3

3.3 Phase Space Plot for File RW20A of the Pilot Cell Test, 48% Alumina . . . . . 3.4

3.4 Phase Space Plot for File RW33A of the Pilot Cell Test, 23% Alumina . . . . . 3.4

3.5 Differential Phase Space Plot for File RW3A of the Pilot Cell Test . . . . . 3.6

3.6 Differential Phase Space Plot for File RW1A of the Pilot Cell Test . . . . . 3.6

3.7 Differential Phase Space Plot for File RW20A of the Pilot Cell Test . . . . . 3.7

3.8 Differential Phase Space Plot for File RW33A of the Pilot Cell Test . . . . . 3.7

3.9 Hurst Plot for File RW1A of the Pilot Cell Test . . . . . 3.9

3.10 Hurst Plot for File RW33A of the Pilot Cell Test . . . . . 3.9

3.11 Hurst Exponents Versus Time Lag for Pilot Cell Test Data . . . 3.10

3.12 A Binomial Fractal Model of Noisy Cell Signals . . . . . 3.10

3.13 Typical Current Measurements in Laboratory Cells . . . . . 3.12

3.14 An Idealized f-Alpha Curve . . . . . 3.14

3.15 Typical f-Alpha Curve Obtained from Laboratory Data . . . . . 3.16

3.16 Variation of the Alpha Ratio Parameter Versus Alumina Concentration at 0.25 $A/cm^2$ . . . . . 3.16

3.17 Variation of the Alpha Ratio Parameter Versus Alumina Concentration at 0.75 $A/cm^2$ . . . . . 3.17

3.18 Multiplier Distribution for 8192 Points . . . . . 3.19

3.19 Binomial f-Alpha Distribution Constructed by Sampling from Figure 3.18 . . . . . 3.20

3.20 Typical Multiplier Distribution for Laboratory Data . . . . . 3.21

3.21 Typical f-Alpha Curve for Laboratory Data Using a Multiplier Distribution such as that Shown in Figure 3.20 . . . . . 3.21

3.22 Typical Results for Alpha Ratio Versus Alumina Concentration for Laboratory Data Using the Probabilistic Multifractal Approach . . . . . 3.23

3.23 Multiplier Distribution for File RW4B of the Pilot Cell Test, 85% Alumina . . . . . 3.23

3.24 Multiplier Distribution for File RW1A of the Pilot Cell Test, 76% Alumina . . . . . 3.24

3.25 Multiplier Distribution for File RW22A of the Pilot Cell Test, 52% Alumina . . . . . 3.24

3.26 Multiplier Distribution for File RW29B of the Pilot Cell Test, 32% Alumina . . . . . 3.25

3.27 f-Alpha Distribution for File RW4B of the Pilot Cell Test, 85% Alumina . . . . . 3.25

3.28 f-Alpha Distribution for File RW1A of the Pilot Cell Test, 76% Alumina . . . . . 3.26

3.29 f-Alpha Distribution for File RW22A of the Pilot Cell Test, 52% Alumina . . . . . 3.26

3.30 f-Alpha Distribution for File RW29B of the Pilot Cell Test, 32% Alumina . . . . . 3.27

3.31 Alpha Ratios Versus Percent Alumina for Pilot Cell Test . . . 3.28

3.32 Alpha Ratios Versus Time for Selected Files from Pilot Cell Test . . . . . 3.29

3.33 Typical Power Spectral Density for Pilot Cell Test Data . . . 3.31

TABLES

2.1 Pilot Cell Test Data Files Collected for Analysis by Chaos Theory . . . . . 2.11

# 1.0 INTRODUCTION

The purpose of the work described in this report was to assess the feasibility of developing a non-intrusive alumina sensor for the Hall-Heroult cells used in the commercial[a] production of aluminum. This report describes results from the analysis of data from two types of experiments: 1) laboratory bench-scale experiments performed at Pacific Northwest Laboratory (PNL)[b] during FY 1990, and 2) a full-scale pilot cell test performed at the Reynolds Metals Company in Sheffield, Alabama, during August 1991.

The primary motivation for developing a new method of sensing the alumina content in an aluminum electrolysis bath originated from the results of previous laboratory tests. Those tests showed that cermet inert anodes required high alumina concentrations (near saturation) in the bath to ensure stable operation over long periods of time. However, a high alumina concentration is exactly the regime where standard alumina sensing methods exhibit their lowest sensitivities. The objective of this work was to find a better approach to sensing the bath alumina at higher (near-saturation) concentrations.

As noted above, it is important that the new method be "non-intrusive." This means that the alumina concentration would be sensed indirectly by measuring the current and voltage imposed on the electrolysis cell. The advantage of such an approach is that no new materials (i.e., probes) need to be introduced into the bath, and thus no new materials interactions or corrosion problems need to be solved.

Classical DSA approaches have been applied to the problem but have shown inadequate sensitivity in the past. The classical approaches employ treatment

---

(a) Since this technology is being evaluated in conjunction with inert anodes, the laboratory cells used in this work differ from the present commercial design in that they use the cermet inert anodes being developed by the Pacific Northwest Laboratory (PNL). These anodes have the nominal composition $NiO-NiFe_2O_4$-17% Cu.

(b) Operated for the U.S. Department of Energy by Battelle Memorial Institute under Contract DE-AC06-76RLO 1830.

of the lower order statistical moments[a] in the data to develop correlations between alumina content and process control variables, such as cell current or voltage. The low sensitivity of measurements in the high alumina regime, when accompanied by the usual experimental noise, can lead to difficulties in deducing an alumina versus process variable correlation that will be useful in industrial practice. From research performed in the past, it was concluded that application of the classical methods did not yield a definite correlation, despite the relatively low noise factor in the laboratory data.

PNL has also sought alternative DSA approaches that would exhibit the needed sensitivity at high alumina concentrations. The methods selected were based on applications of the theory of chaotic phenomena to the analysis of time series data. Chaos theories are a relatively recent development that combines features of classical mechanics with certain aspects of statistical mechanics and topology. The term "chaos" was attached to this combination of sciences in the mid-1970s. For the purposes of this report, chaotic phenomena may be viewed as the manifestation of order within highly nonlinear behavior, in the form of patterns in phase space plots, or in the form of patterns within intermittent (noisy) time series signals. These features will be described in more detail in the following section. However, it is most important at this point to realize the unique feature of the DSA-chaos approach that makes it different from standard DSA methods: the chaos approach generally employs very high order statistical moments in the data base to develop the needed correlations between alumina and process variables, whereas the standard approach employs lower order moments. It was believed that the high order moments could provide the needed sensitive measure of alumina content. Application of these methods to analyze the behavior of aluminum electrolysis cells is the subject of this report.

---

(a) Lower order statistical moments include the mean, standard deviation, kurtosis, etc. Higher order moments do not have common names.

# 2.0 EXPERIMENTAL PROCEDURES

The experimental apparatus and methods employed to collect data during the bench-scale laboratory tests and from the full-scale pilot cell test are described in the following two subsections.

## 2.1 LABORATORY EXPERIMENTS

The laboratory cell used at PNL to collect the bench-scale data is shown in Figure 2.1. An IBM AT computer and an Analog Devices, Inc. RTI-860 high speed simultaneous analog input board (for signal conditioning) were used with the HEM Data Corp. Snapshot Storage Scope software to collect, display, and store the data. The inputs to the IBM AT were current and voltage signals taken from a PAR 173 potentiostat, which was operated in the potentiostatic (potential control) mode in these experiments. The electrochemical cell was similar to that used in previous sensors development work at PNL. It consisted of a graphite crucible that served as the cathode, and a cermet anode (sheathed with boron nitride) of nominal composition $NiO-NiFe_2O_4$-17% Cu (Hart et al. 1987). No reference electrode was employed. The best configuration for reducing instrumental noise was to operate the cathode as the working electrode. Consequently, in this work, the working electrode terminal was connected to the cathode and the counter and reference electrode terminals were connected to the anode. To compensate for this "reverse" configuration, the potential was set at negative potentials in order to drive the cermet electrode anodically. The exposed surface area of the anode was one square centimeter. The initial bath was prepared by mixing appropriate amounts of reagent grade materials to give a bath ratio equal to 1.15: 5.5% (by weight) $CaF_2$, 1.0% $MgF_2$, and the desired concentration of alumina. A temperature controller/furnace/thermocouple was used to control the bath temperature at 983°C. The bath ratio and temperature were effectively constant throughout these short-term experiments. In a given test, the anode was inserted once the bath became molten, the temperature was allowed to re-equilibrate, then the anode was polarized potentiostatically to give the desired current density.

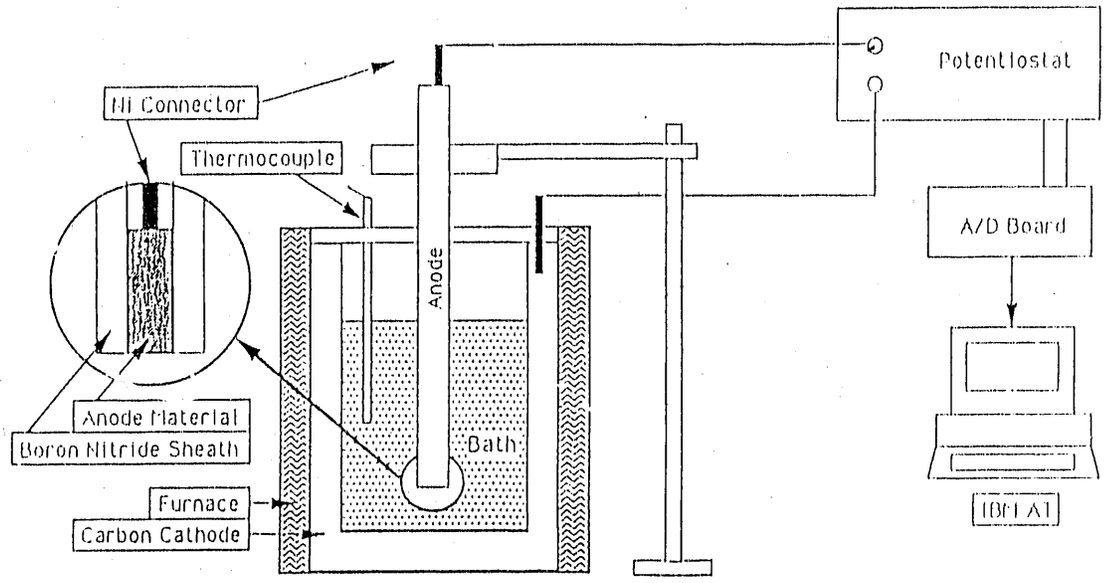


FIGURE 2.1. Apparatus for Collecting Digital Signals from Bench-Scale Aluminum Electrolysis Cells

Current and voltage signals were collected for cells with different alumina concentrations, cell voltage/anode current densities, and anode-to-cathode distances (ACD). These tests were labelled "ACD Tests." Every combination of the following nominal values for these parameters was tested:

Alumina Concentration (weight percent): 0%, 1.5%, 3.0%, 4.5%, 5.1%, 5.6%, and 6.0% (where 8.0% is approximately saturation).

Current Density ($A/cm^2$): 0.25, 0.50, 0.75, and 1.0.

ACD (in.): 3.0, 2.25, 1.5, and 0.75.

Data for a given set of conditions consisted of 10,000 sequential signals collected over a period of 0.5 s (20 KHz sampling frequency). The digital signals were stored as files on 1.4 Mb floppy discs. In addition, for each set of conditions, one file was collected without any additional voltage signal applied, and two files were collected with a ±10 mV AC "ripple" superimposed on the controlling voltage. The frequencies of the ripples were 10 Hz and 1 KHz. These ripple tests were performed to simulate a "noisy cell," as would most likely occur in industrial practice.

Another set of data was also collected. These data, labelled the "DSA Tests," completed the data sets with conditions closer to alumina saturation and over a wider range of alumina concentrations. They employed a ±50 mV ripple instead of the ±10 mV ripple as a possible way to improve sensitivity. The nominal conditions for the DSA tests were:

Alumina Concentration (weight percent): 4.0%, 4.4%, 4.8%, 5.2%, 5.6%, 6.0%, 6.4%, 6.8%, 7.2%, 7.8%, and 8.0%.

Current Density ($A/cm^2$): 0.5 and 0.66.

ACD (in.): 1.5 only.

As in the ACD tests, for each set of conditions one file was collected without any additional voltage signal applied and two files were collected with the ±50 mV ripple at frequencies of 5 and 10 Hz. In addition, another set of files was collected using a standard 2-ohm resistor to determine the extent of instrumental noise. The "resistor data" were collected at current densities of 0.5 and 1.0 $A/cm^2$.

Not all of the above files (over 3 million lines of data) were able to be analyzed using the chaos theory approach because of time and funding limitations. However, enough of the data were analyzed for selected cell conditions to be able to draw conclusions concerning the viability of the four chaos approaches. For example, if the scatter (of a computed parameter) within groups of data at the same alumina concentration was larger than the difference between groups at different concentrations, at the 95% confidence level, then the computed parameter was obviously not suitable as an alumina sensor.

## 2.2 PILOT CELL TEST

The piloted experiment was conducted at the Reynolds Metals Company (RMC) Manufacturing Technology Laboratory in Sheffield, Alabama, during August 1991. The objectives of this test were the pilot-scale evaluation of the inert anode material currently under development at PNL and the collection of data related to the development of a non-intrusive alumina sensor. Although the experimental facilities, methods, and procedures were described in

Windisch et al. (1991), the following abbreviated description of the experimental procedure is included for completeness.

The pilot cell at the RMC facility in Sheffield, Alabama, is a small self-heated, aluminum reduction cell with the capacity for running two industrial-sized carbon anodes. During the pilot cell evaluation of the inert anodes, one industrial-sized carbon anode was run in conjunction with a "six-pack" of inert anodes. The inert anodes had the same composition as the cermet anodes that were evaluated in the laboratory experiments, but were manufactured by Ceramic Magnetics, Inc., of Fairfield, N.J.

The arrangement of the carbon anode and the inert anode cluster is shown in Figure 2.2. The inert anode cluster consisted of six cermet anodes, each with a radius of about 3 in. and a height of 3 in. in the center, with an additional 1-in. lip on the upper edge. All edges were rounded to reduce corner effects.

The electrical buss allowed individual control of the current to the carbon anode and the inert anode cluster. Current through each of the inert anodes could not be controlled separately, but was monitored (through each anode) throughout the test using six 500 A, 100 mV current transducers.

As indicated in the next section, the laboratory test results suggested that better correlations might be obtained by collecting larger data sets (i.e., 50,000 to 100,000 points of simultaneous voltage and current readings) than collected previously in the laboratory experiments. To collect this number of points, data acquisition had to be restricted to one inert anode because the computer memory capacity was limited. Since, even by restricting data collection to one inert anode, only 10,000 data points could be obtained at a time, six successive data acquisitions were performed and then these data were chained together. The resulting data sets (collected over a period of 20 min to half an hour) consisted of 60,000 data points.

The anode in position A (shown in Figure 2.2) was selected for collecting the chaos theory data. The data were collected between August 23 and August 28, 1991, which was the third week of operation with inert anodes. During this time, the actual anode that was in position A was labelled

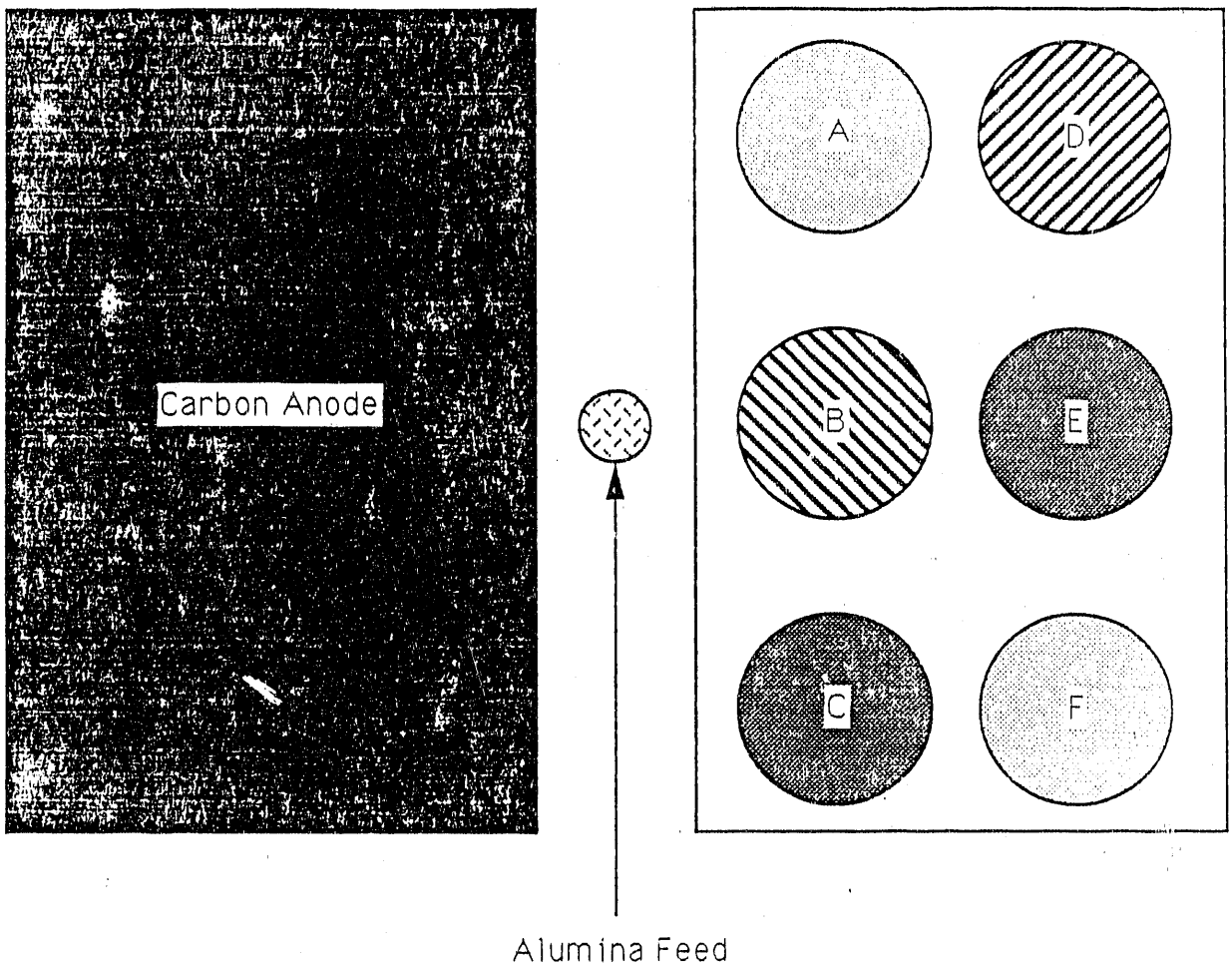


FIGURE 2.2. Top View of Pilot Cell Anodes Showing Relative Anode Positions

Anode E2. Anode E2 was placed into position on August 20, 1991, and was in the pilot cell until the end of the test on August 31, 1991. (For the sake of simplicity, in this report, the anode under study is referred to as Anode A for its position). Between August 23 and August 27, the anode was operated under "normal" conditions, i.e., at about 60 amps and with alumina as close to saturation (about 8 weight percent) as possible. On August 27, alumina feed was stopped and the amount of alumina in the bath began to drop. Data for chaos theory analyses were collected during this time also.

Other conditions for the pilot cell test operation were summarized in Windisch et al. (1991). Analyses of other data from the pilot cell test are

not yet complete but indicate numerous other variations of operating conditions with time (other than alumina concentration) that may have affected the results of this signal analysis study. A complete analysis of the effects of these other variations is beyond the scope of this initial study, but for the sake of completeness, it is worth noting that they included variations in ACD and the depth of immersion, variation of current and potential on the carbon anode and on other inert anodes, variations in bath properties due to ledge formation and mucking, and significant changes in the anode itself due to corrosion.

The pilot cell power supplies were essentially unfiltered DC (actually, 6-phase rectified AC) output units capable of thousands of amps in the 5 to 10 volt range. The supplies "floated" with respect to the building electrical ground, so common mode voltages existed that were not controlled. The pilot cell voltage and current signals were derived from dividers and shunts connected directly to the pilot cell, and so floated with it. This electrically noisy environment and the heat generated by the pilot cell during operation, combined with the naturally occurring heat and humidity of summer in Alabama, presented a challenge to accurate data acquisition. An additional problem was that the recording computer was operated from a room about 100 ft from the pilot cell, requiring a long cable to connect it to the signal sources.

The equipment for data collection is shown in the block diagram in Figures 2.3a and 2.3b. The equipment included an IBM AT and an Analog Devices RTI-860 high-speed simultaneous analog input board with Analog Devices 3B40-00 and 3B41-00 isolation amplifiers. HEM Data Corp. Snapshot Storage Scope software was used to collect, display, and store the data. Inputs to the signal conditioning modules were available over 16 channels. Two of the channels were used for collecting the chaos theory data: a) one channel for the current through Anode A and b) one channel for the voltage between the electrical tap at the top of Anode A and the cathode voltage tap. The remaining 14 channels were available for collecting data for other signal analysis studies during the pilot cell test.

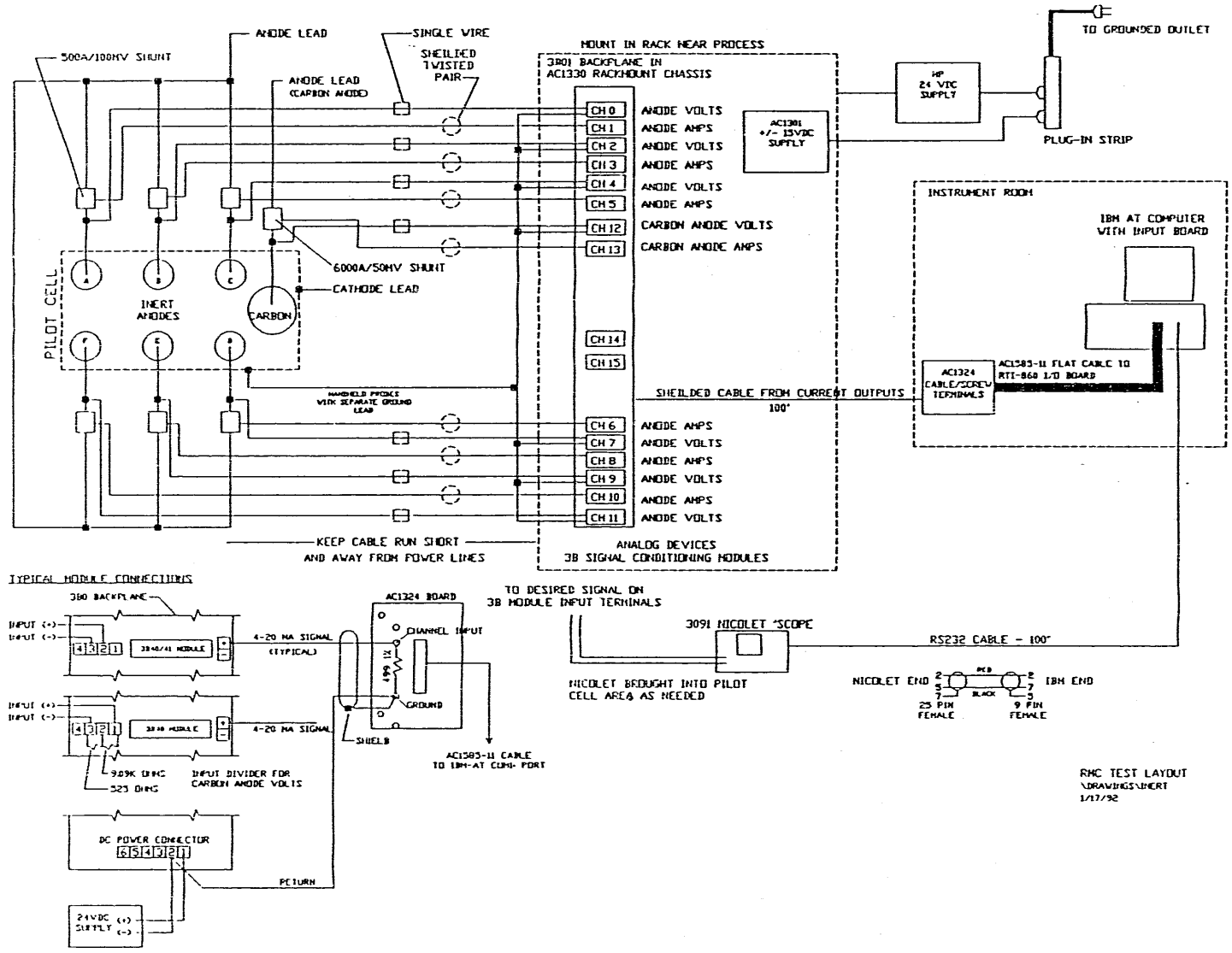


FIGURE 2.3a. Block Diagrams of Signal Acquisition System for Pilot Cell Test

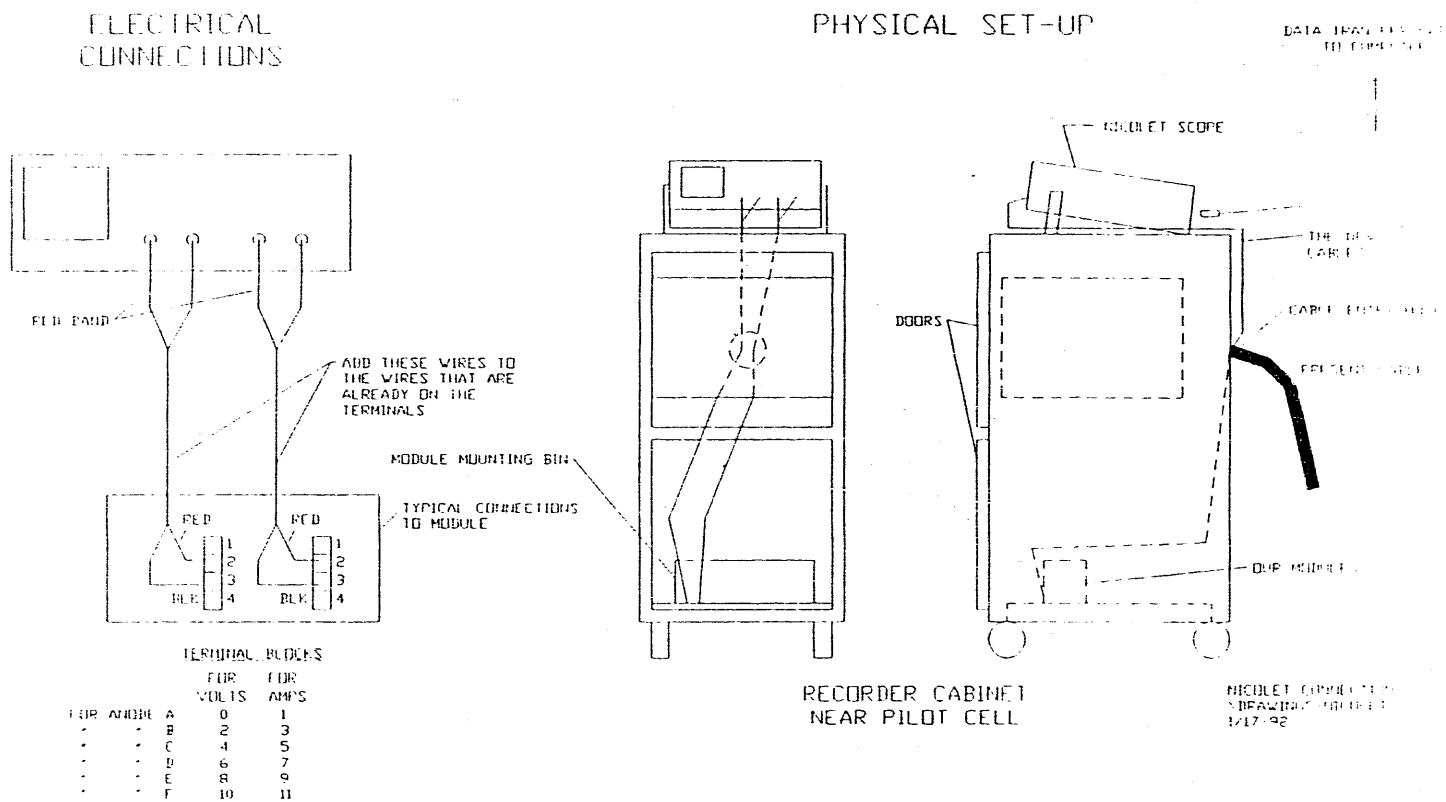


FIGURE 2.3b. Block Diagrams of Signal Acquisition System for Pilot Cell Test

The amplifiers had an isolated, floating input that allowed direct attachment to the voltage dividers and shunts on the pilot cell without concern for ground loops or common mode voltages. The nominal 0-10 kHz bandwidth of the amplifiers was reduced to 0-25 Hz (3 dB point) using plug-in filters. This bandwidth selection was based on previous experiments, which indicated that all useful sensor frequency data occurred below 25 Hz.

The output of the amplifiers was not isolated, nor was the input on the computer. The approximately 100 ft of cable run between the two units allowed both induced and common mode noise to cause problems. These problems were nearly eliminated by selecting an amplifier's current output rather than its voltage output. Experimenting with combinations of the grounding location of the output cable shield and the AC power outlet used for the amplifiers eliminated the rest of the noise.

The current signal from the isolation amplifiers was changed to a voltage signal with a resistor mounted at the input to the analog data input board used in the computer. By making the conversion at the computer input, the effect of any voltage drop or induced voltages along the cable was eliminated. This would not have been possible using a voltage signal from the amplifiers.

The Analog Devices RTI-860 data acquisition board provided 16 channels, as indicated above, with 12 bit resolution (1 part in 4096) at rates up to 200 kHz per channel. For the chaos theory analysis, data were collected from the single inert anode position A at 20 kHz over a period of 0.5 s (for a total of 10,000 current and voltage measurements). The 20-kHz sampling frequency was sufficiently higher than the 25-Hz bandpass of the amplifiers to avoid "aliasing" effects, but low enough to keep data files from exceeding the computer and software limitations. The board was mounted in the IBM AT which ran the software for data acquisition, scaling, and file storage.

In some of the analyses reported here, a correction was applied to the voltage data. This was done to see if the sensitivity of the data to alumina concentration could be improved by subtracting out components of the voltage known (or suspected) to be independent of alumina. In cases where the correction was applied, two components of the voltage were removed: the voltage drop through the connector rod ($V_c$) and the back emf of the anode ($V_b$):

$$V = V_m - V_c - V_b \tag{2.1}$$

where V is the voltage used in the analysis and $V_m$ is the measured voltage.

$V_c$ was calculated using the equation

$$V_c = 0.002I \tag{2.2}$$

where I is the current through anode A. The factor 0.002 was derived from an independent measurement of resistance through the connector rod. $V_b$ was obtained by extrapolating (assuming linearity) a volt-amp curve for anode A to zero current. During the time the chaos theory data were collected, $V_b$ was found to be 3.70 Volts. The reason $V_b$ is significantly larger than the reversible potential for the electrode reaction (2.20 V) is because of the influence of the large carbon anode in the cell. During these measurements, the carbon anode was operating at 3.5 KAmps.

Data collected from the test cell included the current for anode A and the voltage between the top of the connector rod for Anode A and the electrical connection at the cathode. The current and voltage signals were collected simultaneously at 20 kHz over a 0.5-s interval (10,000 data points) and stored in files on a 1.4 Mb floppy discs. There were six such files collected within 30 min at each data recording session, and a total of 16 such sessions for the chaos theory data. The alumina concentration was measured as weight percent by sampling the bath. The weight percent values were converted to percent saturations (of alumina in the bath under each set of temperature/bath conditions during which the sample was taken) using the formula by E. Skybakmoen et al. (1990). The alumina concentration was assumed not to vary significantly over the period of a recording session. The data base is shown in Table 2.1. A plot of the percent saturation of alumina versus time (days from start of the test) is shown in Figure 2.4. Only data for which chaos theory data were collected are shown. "Day 20" corresponds to August 23, 1991, at about 10 a.m.

TABLE 2.1. Pilot Cell Test Data Files Collected for Analysis by Chaos Theory

| Date | Time | Name | Nom. Volts | Nom. Amps | %Alumina | Comments |
|---|---|---|---|---|---|---|
| 8/23 | 0929 | RW1A | 6.14 | 80 | 76.55 | |
| | 0935 | RW1B | 6.12 | 80 | 76.55 | |
| | 0939 | RW1C | 5.97 | 80 | 76.55 | |
| | 0943 | RW2A | 5.90 | 83 | 76.55 | |
| | 0947 | RW2B | 5.83 | 83 | 76.55 | |
| | 0951 | RW2C | 6.21 | 83 | 76.55 | |
| 8/24 | 1007 | RW3A | 5.16 | 72 | 85.25 | E&F Out |
| | 1012 | RW3B | 5.11 | 69 | 85.25 | E&F Out |
| | 1017 | RW3C | 5.09 | 69 | 85.25 | E&F Out |
| | 1021 | RW4A | 5.09 | 69 | 85.25 | E&F Out |
| | 1026 | RW4B | 5.09 | 69 | 85.25 | E&F Out |
| | 1030 | RW4C | 5.14 | 68 | 85.25 | E&F Out |
| 8/24 | 1355 | RW5A | 5.24 | 66 | 84.95 | E Out |
| | 1401 | RW5B | 5.18 | 66 | 84.95 | E Out |
| | 1406 | RW5C | 5.17 | 68 | 84.95 | E Out |
| | 1411 | RW6A | 5.16 | 67 | 84.95 | E Out |
| | 1416 | RW6B | 5.14 | 65 | 84.95 | E Out |
| | 1420 | RW6C | 5.14 | 68 | 84.95 | E Out |
| 8/25 | 0733 | RW7A | 4.74 | 58 | 79.80 | |
| | 0738 | RW7B | 4.78 | 57 | 79.80 | |
| | 0743 | RW7C | 4.80 | 58 | 79.80 | |
| | 0747 | RW8C | 4.79 | 58 | 79.80 | |
| | 0753 | RW8B | 4.77 | 57 | 79.80 | |
| | 0757 | RW8C | 4.80 | 56 | 79.80 | |
| 8/25 | 1603 | RW9A | 5.68 | 68 | 83.30 | |
| | 1608 | RW9B | 5.67 | 69 | 83.30 | |
| | 1612 | RW9C | 5.64 | 70 | 83.30 | |
| | 1616 | RW10A | 5.66 | 71 | 83.30 | |
| | 1620 | RW10B | 5.65 | 73 | 83.30 | |
| | 1625 | RW10C | 5.63 | 70 | 83.30 | |

TABLE 2.1. (contd)

| Date | Time | Name | Nom. Volts | Nom. Amps | %Alumina | Comments |
|---|---|---|---|---|---|---|
| 8/26 | 0955 | RW11A | 6.18 | 59 | 84.60 | |
| | 1001 | RW11B | 6.17 | 58 | 84.60 | |
| | 1009 | RW11C | 6.63 | 56 | 84.60 | |
| | 1015 | RW12A | 6.84 | 53 | 84.60 | |
| | 1021 | RW12B | 6.05 | 54 | 84.60 | |
| | 1025 | RW12C | 5.60 | 42 | 84.60 | |
| 8/26 | 1724 | RW13A | 5.18 | Unknown | 82.10 | B Out |
| | 1728 | RW13B | 5.17 | Unknown | 82.10 | B Out |
| | 1732 | RW13C | 4.92 | Unknown | 82.10 | B Out |
| | 1737 | RW14A | 4.93 | Unknown | 82.10 | B Out |
| | 1742 | RW14B | 4.90 | Unknown | 82.10 | B Out |
| | 1745 | RW14C | 4.96 | Unknown | 82.10 | B Out |
| Alumina Feed Stopped at 0400 Hrs on 8/27 | | | | | | |
| 8/27 | 0921 | RW16A | 4.94 | 55 | 48.46 | B Out |
| | 0926 | RW16B | 4.89 | 53 | 48.46 | B Out |
| | 0930 | RW16C | 5.00 | 68 | 48.46 | B Out |
| | 0934 | RW17A | 5.01 | 61 | 48.46 | B Out |
| | 0939 | RW17B | 5.00 | 57 | 48.46 | B Out |
| | 0943 | RW17C | 4.96 | 61 | 48.46 | B Out |
| 8/27 | 1038 | RW18A | 5.01 | 57 | 48.46 | B Out |
| | 1042 | RW18B | 5.01 | 57 | 48.46 | B Out |
| | 1046 | RW18C | 5.01 | 57 | 48.46 | B Out |
| | 1052 | RW19A | 5.23 | 67 | 48.46 | B Out |
| | 1056 | RW19B | 5.29 | 72 | 48.46 | B Out |
| | 1101 | RW19C | 5.27 | 68 | 48.46 | B Out |
| 8/27 | 1216 | RW20A | 5.29 | 69 | 48.46 | B Out |
| | 1221 | RW20B | 5.27 | 68 | 48.46 | B Out |
| | 1225 | RW20C | 5.28 | 69 | 48.46 | B Out |
| | 1232 | RW21A | 5.25 | 65 | 48.46 | B Out |
| | 1237 | RW21B | 5.22 | 67 | 48.46 | B Out |

TABLE 2.1. (contd)

| Date | Time | Name | Nom. Volts | Nom. Amps | %Alumina | Comments |
|---|---|---|---|---|---|---|
| 8/27 | 1242 | RW21C | 5.26 | 68 | 48.46 | B Out |
| 8/27 | 1412 | RW22A | 5.75 | 82 | 52.24 | B Out |
| | 1417 | RW22B | 5.73 | 80 | 52.24 | B Out |
| | 1421 | RW22C | 5.62 | 78 | 52.24 | B Out |
| | 1426 | RW23A | 5.59 | 78 | 52.24 | B Out |
| | 1431 | RW23B | 5.60 | 70 | 52.24 | B Out |
| | 1436 | RW23C | 5.54 | 78 | 52.24 | B Out |
| 8/27 | 1556 | RW24A | 5.29 | 74 | 53.75 | B Out |
| | 1600 | RW24B | 5.21 | 71 | 53.75 | B Out |
| | 1604 | RW24C | 5.22 | 71 | 53.75 | B Out |
| | 1610 | RW25A | 5.22 | 70 | 53.75 | B Out |
| | 1615 | RW25B | 5.30 | 72 | 53.75 | B Out |
| | 1619 | RW25C | 5.32 | 71 | 53.75 | B Out |
| 8/27 | 1954 | RW26A | 5.24 | 78 | 47.46 | B Out |
| | 1958 | RW26B | 5.37 | 82 | 47.46 | B Out |
| | 2002 | RW26C | 5.38 | 82 | 47.46 | B Out |
| | 2007 | RW27A | 5.34 | 83 | 47.46 | B Out |
| | 2011 | RW27B | 5.34 | 83 | 47.46 | B Out |
| | 2016 | RW27C | 5.30 | 82 | 47.46 | B Out |
| 8/28 | 0859 | RW29A | 5.65 | 59 | 31.82 | B Out |
| | 0904 | RW29B | 5.67 | 57 | 31.82 | B Out |
| | 0908 | RW29C | 5.63 | 57 | 31.82 | B Out |
| | 0913 | RW30A | 5.78 | 67 | 31.82 | B Out |
| | 0918 | RW30B | 5.08 | 72 | 31.82 | B Out |
| | 0922 | RW30C | 5.64 | 68 | 31.82 | B Out |
| 8/28 | 1112 | RW31A | 5.36 | 77 | 31.82 | B Out |
| | 1116 | RW31B | 5.38 | 76 | 31.82 | B Out |
| | 1120 | RW31C | 5.34 | 77 | 31.82 | B Out |
| | 1125 | RW32A | 5.37 | 75 | 31.82 | B Out |

TABLE 2.1. (contd)

| Date | Time | Name | Nom. Volts | Nom. Amps | %Alumina | Comments |
|---|---|---|---|---|---|---|
| 8/28 | 1130 | RW32B | 5.36 | 75 | 31.82 | B Out |
| | 1134 | RW32C | 5.34 | 76 | 31.82 | B Out |
| 8/28 | 1321 | RW33A | 5.19 | 80 | 23.00 | B Out |
| | 1326 | RW33B | 5.03 | 80 | 23.00 | B Out |
| | 1330 | RW33C | 5.03 | 80 | 23.00 | B Out |
| | 1334 | RW34A | 5.15 | 83 | 23.00 | B Out |
| | 1334 | RW34B | 5.15 | 84 | 23.00 | B Out |
| | 1344 | RW34C | 5.21 | 83 | 23.00 | B Out |

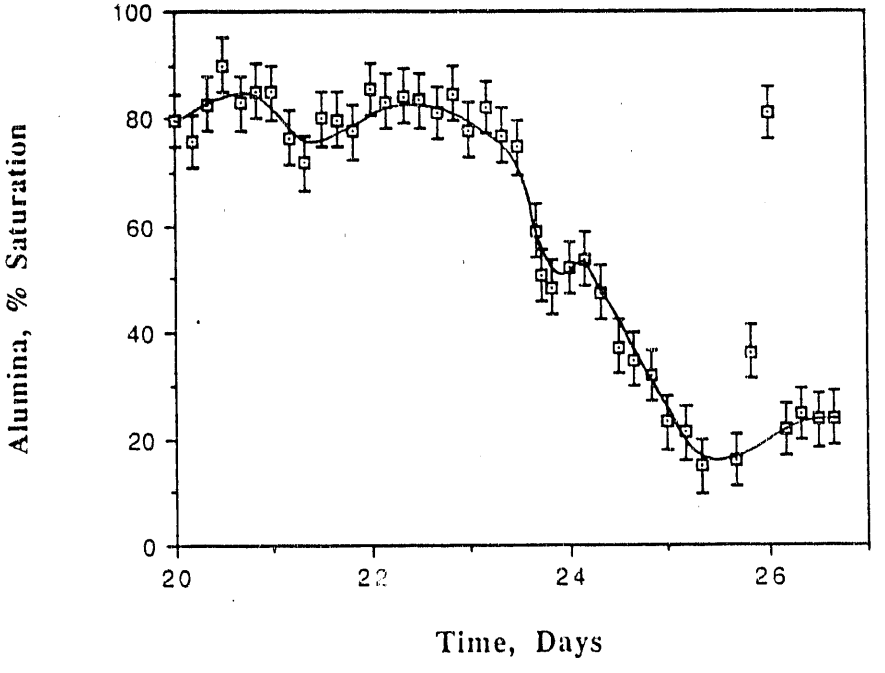


FIGURE 2.4. Alumina Concentration Versus Time for the Pilot Cell Test

## 3.0 DATA ANALYSIS USING CHAOS THEORY

The four approaches to data analysis using chaos theory are described in the following subsections. In each case, these descriptions are followed immediately by the results obtained from the laboratory data and from the pilot cell data, although not necessarily in the chronological order of application.

### 3.1 PHASE SPACE PLOTS

The foundations of this approach originate from classical mechanics, where phase space plots have long been used to study complicated dynamical systems. "Phase space" means that the variables of a process are plotted against each other, e.g., the position of a pendulum versus its velocity. The resulting plots often exhibit certain specific patterns, such as a spiral for a damped pendulum. If the system is "chaotic," the pattern may be more complex, but nevertheless recognizable, and is called a "strange attractor." This means that the system is dynamically attracted to a specific set of "orbits" or to a specific region of phase space. An example is the famous Lorentz attractor, which resembles a butterfly or an owl's mask.

Phase space plots were envisioned as the simplest approach to employ. They were the context in which applications of chaos theories to an alumina sensor were first discussed. Because simple solutions are easier to apply in industrial practice, this method was attempted first. Conceivably, a plant operator could monitor a "pattern" on a video screen. A certain pattern indicative of acceptable alumina content would signify proper cell operating conditions. Any deviation from this pattern would alert the operator to make sufficient adjustments in alumina concentration to bring the pattern back to "normal." High-speed data acquisition, processing, and display would be required to facilitate such an operation.

The phase space approach involves plotting the cell electrical resistance (R) at time t versus the resistance at time t+1, or t+2, etc. This is also sometimes known as a "characteristic diagram" in classical Fourier

analyses. Resistance was computed by simply dividing the instantaneous cell voltage by the instantaneous current, and plotting the results as described below.

### 3.1.1 Results for Laboratory Experiments

The expectation was that some recognizable pattern would emerge as a function of alumina content. However, no such pattern could be found. The plots appeared equally scattered, with a generally higher data point density along a line at a 45 degree angle across the plot area. Although further analysis using the method of Poincare sections (a slice through the data perpendicular to the plane of the plot) could have been attempted to search for such patterns, the approach did not appear to be promising given the appearance of the phase space plots. It was decided that the next stage of analysis would address the full spectrum of R(t) versus R(t+b) correlations (where b varies by several orders of magnitude) that were possible in the laboratory data base. The results of that effort are described in Section 3.2.1.

### 3.1.2 Results for Pilot Cell Test

Two series of phase space plots were generated from the pilot test data, as follows. The first series consisted of a set of standard plots for the raw data, corrected for the voltage drop through the anode connection and the back emf as described in Section 2.2. Representative results are shown in Figures 3.1 to 3.4 for alumina concentrations of 85%, 76%, 48%, and 23% of saturation, respectively. It is apparent that a distinctive pattern has occurred for these data. This pattern could be recognizable and useful to an operator in an industrial setting if it also exhibited consistent changes as the alumina content changed. However, this was not the case: Figures 3.1 to 3.4 show only one of the many observed pattern changes as a function of alumina content. It must be noted that any minor differences that may be seen in these plots are due to scatter in the data, rather than a discernable correlation versus alumina content. For example, there is no significant difference between Figure 3.1 (85% alumina) and Figure 3.4 (23% alumina).

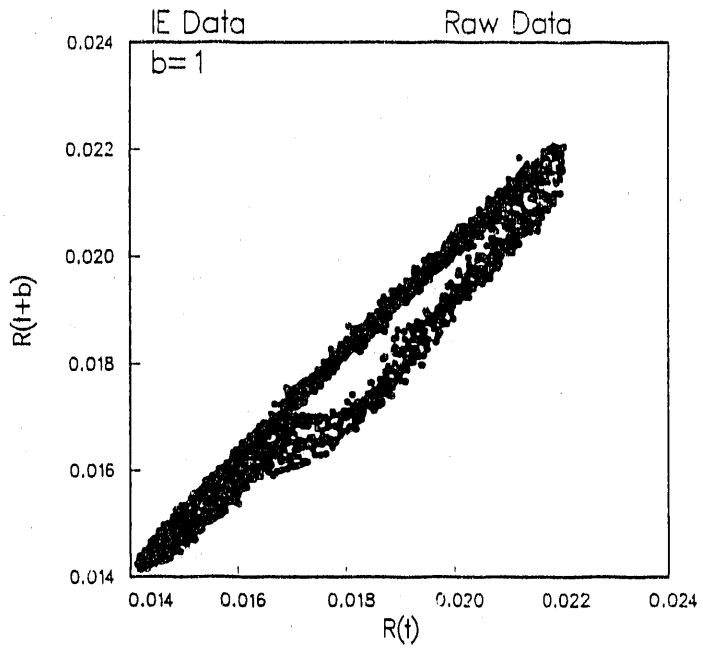


FIGURE 3.1. Phase Space Plot for File RW3A of the Pilot Cell Test, 85% Alumina

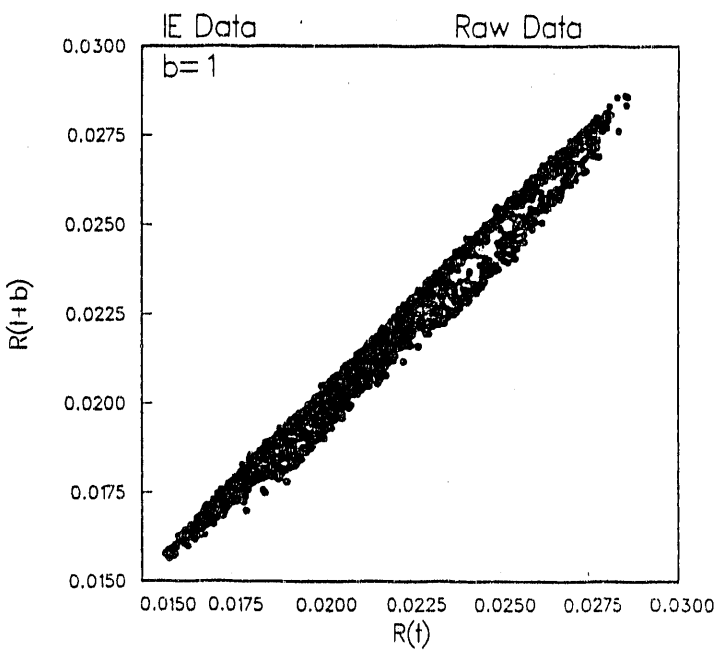


FIGURE 3.2. Phase Space Plot for File RW1A of the Pilot Cell Test, 76% Alumina

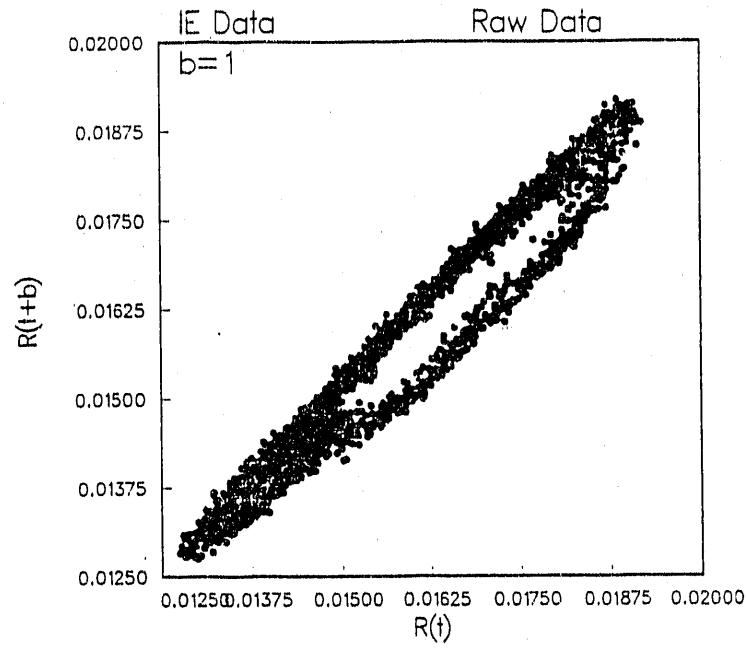


FIGURE 3.3. Phase Space Plot for File RW20A of the Pilot Cell Test, 48% Alumina

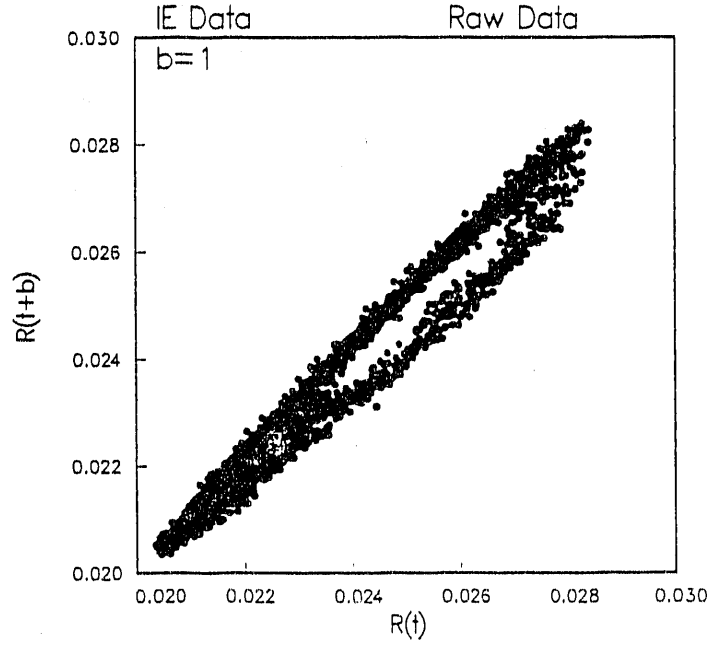


FIGURE 3.4. Phase Space Plot for File RW33A of the Pilot Cell Test, 23% Alumina

The same conclusions can be reached from the second series (Figures 3.5 to 3.8, which are phase space plots constructed from the derivatives of the above plots. This variation of the method was attempted in an effort to amplify any differences in the above plots.

## 3.2 HURST EXPONENTS

This method has its basis in about 2000 years of observations of climatologic and hydrologic trends throughout the world. It was first formally investigated by Hurst (1951), who empirically correlated these observations in terms of simple statistical parameters:

$$R/\sigma = (\tau/2)^H \tag{3.1}$$

where R is the range of observations, $\sigma$ is the standard deviation, $\tau$ is the time lag between observations, H is the Hurst exponent, and $0<H<1$. For $H = 0.5$, the process is entirely analogous to a random walk, as in diffusion processes where the variable $(Dt)^{0.5}$ occurs. For $0.0<H<0.5$, the process tends to overcompensate by frequent reversals of direction, and a "noisy" curve occurs (called "antipersistent"). For $0.5<H<1.0$, a smoother, less noisy curve occurs, and the process is called "persistent" because it exhibits a general increasing or decreasing trend that only occasionally reverses direction. Most natural processes, such as regional rainfalls, exhibit an H of about 0.72.

### 3.2.1 Results for Laboratory Tests

The PNL laboratory data were analyzed using the Hurst concept, varying $\tau$ over five orders of magnitude. The results suggested that the electrolysis processes were antipersistent (noisy) in the short term (small $\tau$), but persistent (controlled) in the long term. These results were not surprising, however. They can be deduced by simply watching the process in practice. The signals are noisy, but the process remains under control.

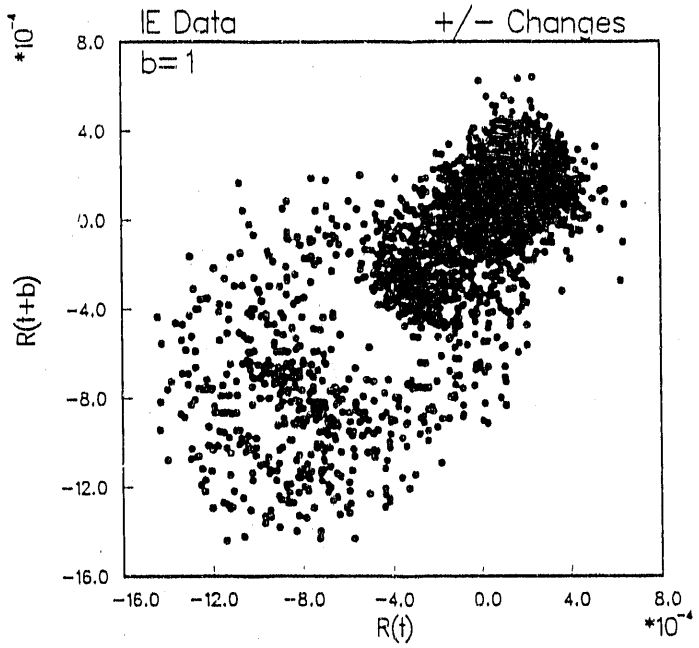


FIGURE 3.5. Differential Phase Space Plot for File RW3A of the Pilot Cell Test

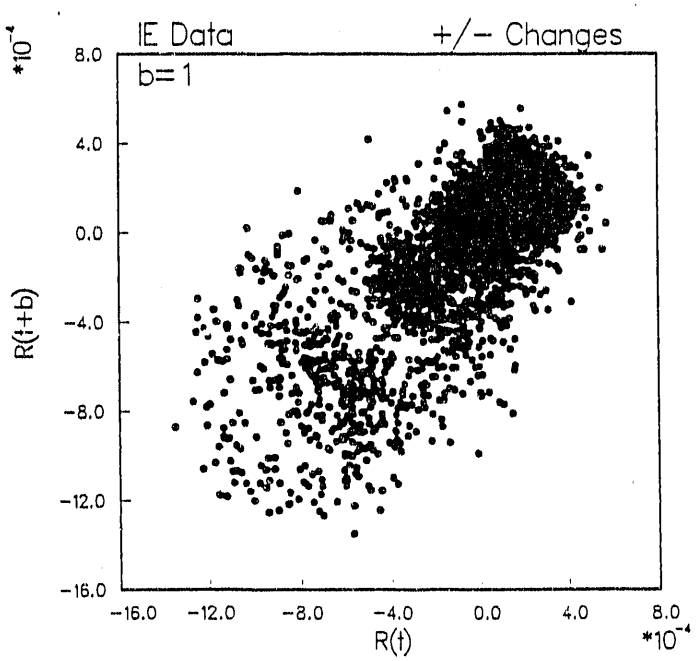


FIGURE 3.6. Differential Phase Space Plot for File RW1A of the Pilot Cell Test

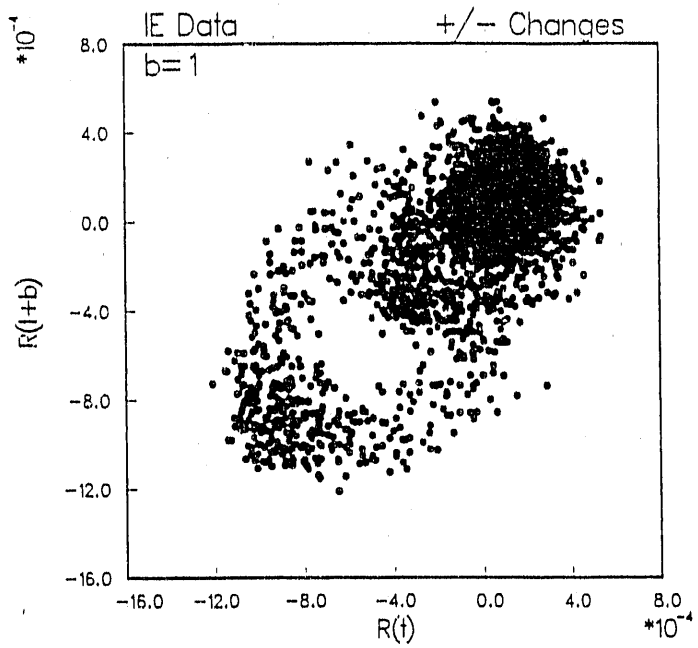


FIGURE 3.7. Differential Phase Space Plot for File RW20A of the Pilot Cell Test

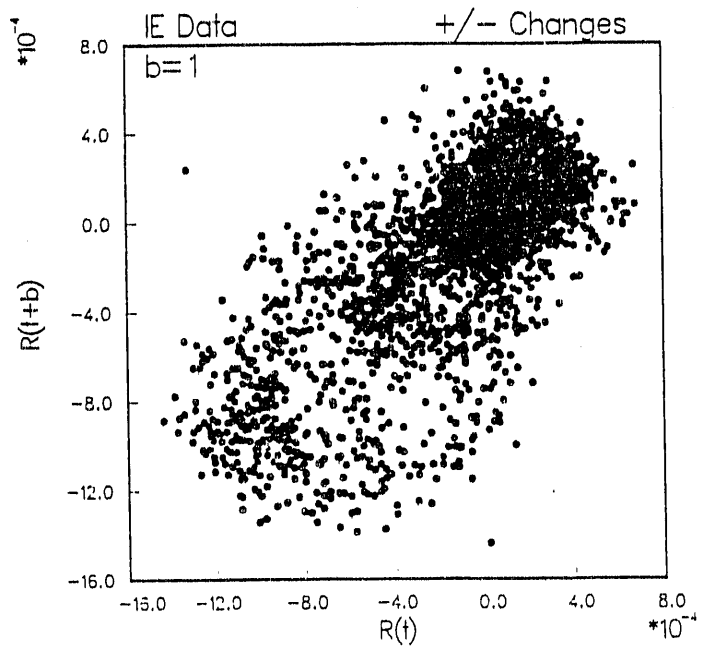


FIGURE 3.8. Differential Phase Space Plot for File RW33A of the Pilot Cell Test

### 3.2.2 Results for Pilot Cell Test

Figures 3.9 and 3.10 show plots of data analyzed using Equation (2.2) for the first and last data files, at 76% and 23% alumina, respectively. The averaged value of H (slope of the curve in the figures) is not significantly different for these two cases, indicating a lack of sensitivity with respect to alumina concentration, or a small signal-to-noise ratio.

Figure 3.11 shows a plot of H versus the time lag $\tau$. This plot exhibits classic behavior in that H generally decays from a high value of about 0.9 at small time lags, to an H of about 0.5 at long time lags. The high H at small lags indicates a high "memory" of events that occurred a short time in the past, and an H approaching 0.5 indicates that the system exhibits random behavior at long time lags, with no memory of past events. $\tau$ = 500 corresponds to about 25 m sec.

It is interesting to note that effect of the period of the six-phase rectifier (operating at 60 Hz with a period of 2.8 milliseconds) on the anode is clearly detected at a time lag of about 50 data points (2.5 milliseconds). This is the only exception to the otherwise standard appearance of the H versus time lag plot. Although it does serve as a check that the Hurst method is working properly, the rectifier period has no relationship to the alumina content. Consequently, these results gave no new information that could be used to develop a non-intrusive alumina sensor.

## 3.3 MULTIFRACTALS

Since the simpler chaos-related approaches described above were either not promising or gave self-evident results, it was necessary to implement more complicated mathematical methods. These methods fall under the category called "multifractals." After a brief outline of fractal concepts, the two multifractal approaches employed in this effort are described.

A fractal is a geometric object with non-integer dimension. That is, it describes geometric complexity in terms of transitions between the Euclidean integer dimensions. The same concepts also apply to time series plots, a simple model for which is shown in Figure 3.12. In this case, the total

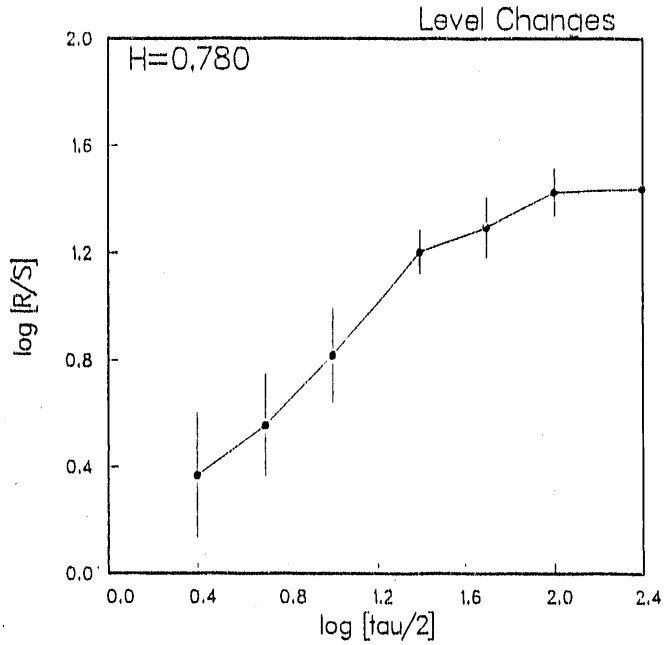


FIGURE 3.9. Hurst Plot for File RW1A of the Pilot Cell Test

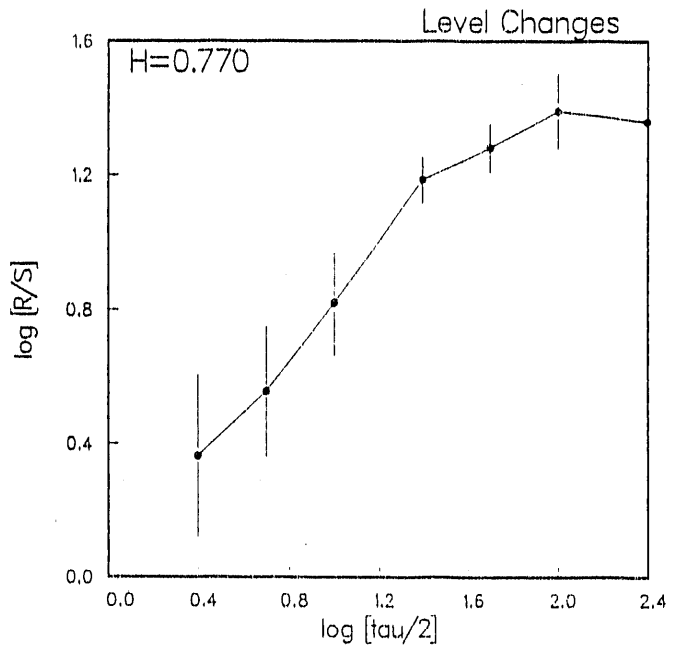


FIGURE 3.10. Hurst Plot for File RW33A of the Pilot Cell Test

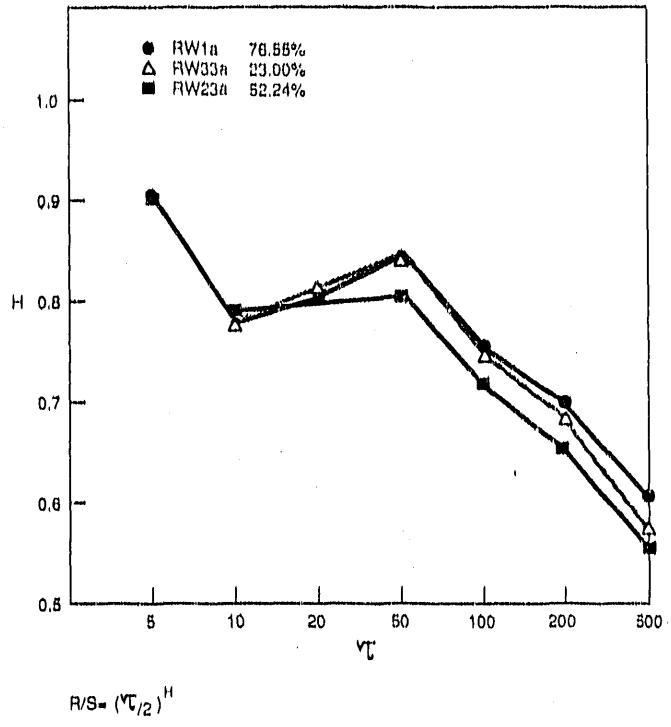


FIGURE 3.11. Hurst Exponents Versus Time Lag for Pilot Cell Test Data

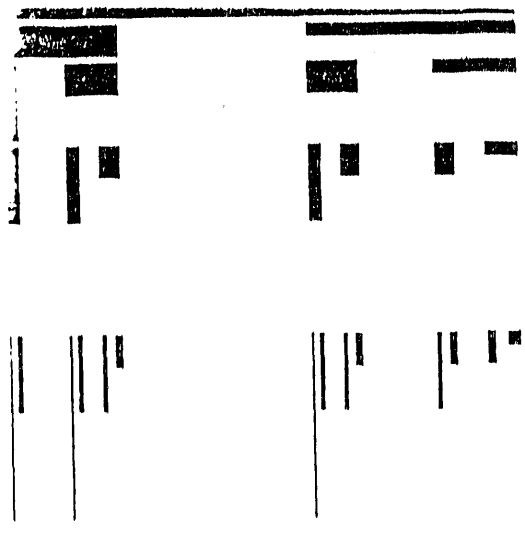

FIGURE 3.12. A Binomial Fractal Model of Noisy Cell Signals

signal (resistance integrated over time) is divided up as follows. The area of the bar at the top of the figure is the total integrated resistance over a time t (the length of the bar). It is divided up into two parts in the second line in Figure 3.12: the bar on the left is 25% as long as the original bar, and the bar on the right is 40% as long. Sixty percent of the area is assigned to the left bar, and 40% to the right bar, thus conserving the total bar area (integrated signal). This process is repeated again on the next line, and so on. The result is that the total signal is redistributed on a broken-up line called a Cantor bar. This is also a model for intermittent or noisy time series, where the length represents time, and the signal spikes are thus distributed over time in a fractal fashion. Since the horizontal axis was divided into two parts, the cell dynamics are thus being modeled by a binary process. If Figure 3.12 is turned upside down and some randomness is included, the resemblance to the cell current versus time in Figure 3.13 is obvious. This similarity provided the motivation for attempting this method. By embedding a large number of fractals (such as shown in Figure 3.12) within each other, a multifractal is constructed, and a typical noisy time series plot can be produced that more closely resembles the actual data.

An important question is just how multifractals can be used to unravel information from a noisy time series plot and use it to develop an alumina sensor. There are two ways to approach this: a thermodynamic way and a probabilistic way. These are described in the following subsections, along with results from their applications to the data.

### 3.3.1 Thermodynamic Formalism

Halsey et al. (1986) published a paper that describes the thermodynamic method, which is essentially the reverse of the above embedding procedure. In this approach (whose only description possible is mathematical), the generalized dimensions ($D_q$) are first defined, based on the generalized entropies (Frisch and Parisi 1985):

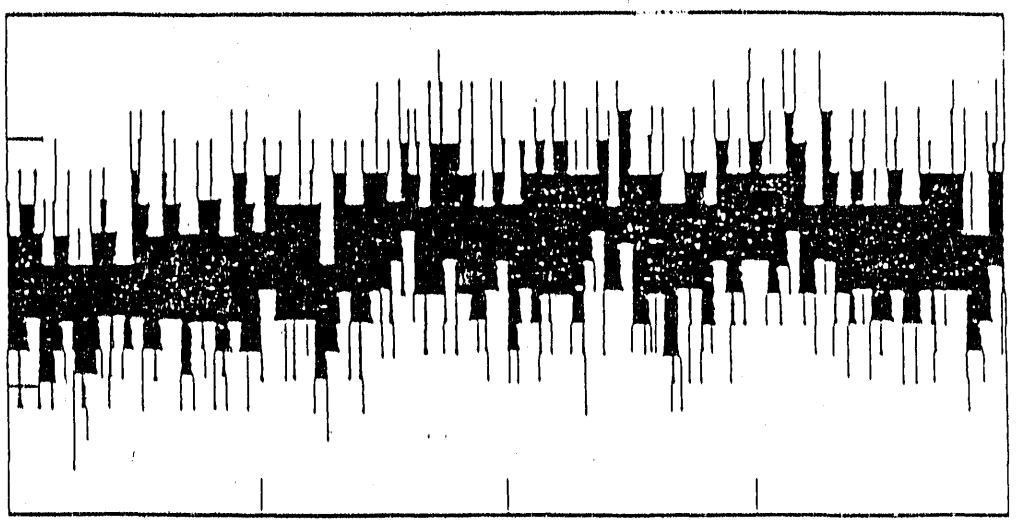

time

FIGURE 3.13. Typical Current Measurements in Laboratory Cells

$$D_q = \frac{1}{q-1} \lim_{b \to 0} \frac{\ln \sum P^q(b)}{\ln(b)} \tag{3.2}$$

where q is the order of the moment ($-\infty<q<\infty$) and is analogous to the inverse temperature ($\beta = 1/kT$) of statistical thermodynamics, and P(b) is the measure (total integrated cell resistance) in a "box" of size b within the time series. The keys to the analysis are two-fold: 1) P is normalized to unity, as in probability theory, and 2) the box size b varies over at least three decades. The mechanics of computing $D_q$ from the cell time series data involves dividing the normalized total resistance into boxes of size b1, then of b2<b1, etc., and computing the above limit. This is described by Meneveau and Sreenivasan (1987) in modeling turbulent flows.

The next steps are to define the "mass exponent" ($\tau$):

$$\tau = (1 - q)\ D_q \tag{3.3}$$

and the "free energy" ($\alpha$):

$$\alpha = \partial\tau/\partial q \tag{3.4}$$

and then to combine these in a Legendre transform to get the "entropy" (f):

$$f = q\alpha - \tau \tag{3.5}$$

Note that there is a range of alpha values and a range of f values, each pair of f-alpha values corresponding to a particular moment q. Although each f is thermodynamically an entropy, it is also the dimension of one of the "nested" fractals (Figure 3.12) that make up the entire multifractal structure.

The truly remarkable result of Halsey's paper is that when f is plotted versus alpha, a "universal" curve is found for an extraordinarily large variety of data bases and physical phenomena. Such an f-alpha curve is sketched in Figure 3.14, and has the following general features. At the top of the unimodal curve, the value of f is $D_0$, the zeroth order moment in the data. $D_0$ is also the fractal dimension of the overall structure, and is the dimension that is most familiar in the literature. All other f values are the dimensions of fractal sets embedded within the overall multifractal. Most interesting is the value at q=1, where $D_1$ is formally Shannon's information entropy. It has also been used as the fractal dimension of fracture surfaces (e.g., Williford 1988).

It is noteworthy that $D_0$ and $D_1$ are essentially invariant (always the same for a given phenomenon) if the data are normalized as described above. The result is a lack of sensitivity for lower order moments in the data, which also impacts the classical DSA methods as discussed in the Introduction.

The intercepts of the curve in Figure 3.14 with the horizontal axis define two values of alpha. These values, $\alpha_{min}$ and $\alpha_{max}$, are the dimensions of the two competing energetic processes that form the binomial distribution. They produce the apparently chaotic time series signal because of their competition for dominance. In essence, the electrode/electrolyte system could be

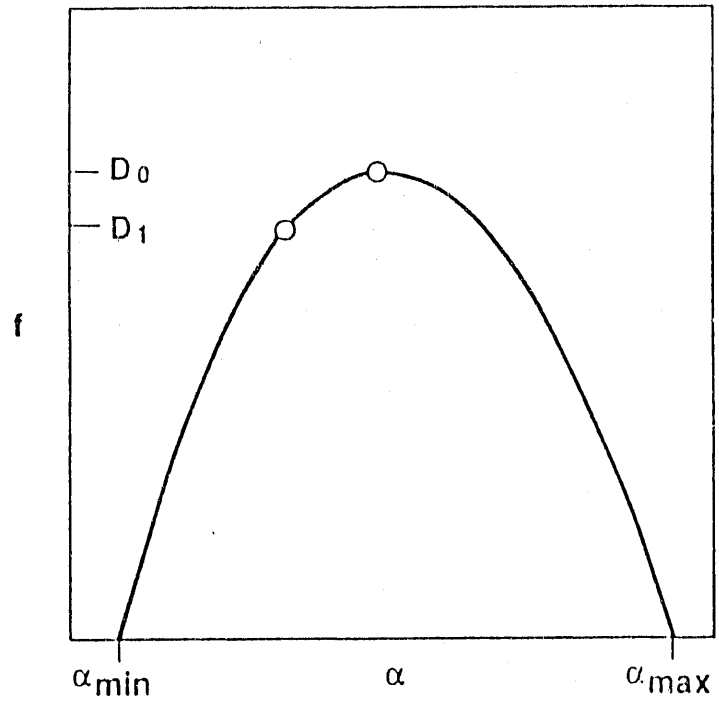


FIGURE 3.14. An Idealized f-Alpha Curve

viewed as undergoing a bistable process that hops back and forth between these two more fundamental processes. Examples of two processes that may contribute (but whose roles are not proven here) are anode film formation/dissolution, or bath bubble formation/collapse. It is the values of $\alpha_{min}$ and $\alpha_{max}$ that describe the high order moments in the data base, and hence are unique to the multifractal DSA methods.

Results for Laboratory Tests

Although several mathematical combinations of $\alpha_{min}$ and $\alpha_{max}$ could be employed as a measure of alumina content, the ratio $\alpha_{max}/\alpha_{min}$ was selected because it simplified the analysis, as follows. Note that $\alpha_{min} = \ln(P_{max})/\ln(b)$ and $\alpha_{max} = \ln(P_{min})/\ln(b)$, where $b<<1$ and $0<P<1$. If the dynamics of the process are rapid enough so that the two competing processes may occur on the same substructure (i.e., for the same value of b, where $b = 1/l$ and $l$ is the characteristic size of the electrode roughness, or bath bubble, etc.),

then the variable b cancels out of the resulting alpha ratio. This gives a correlation parameter involving only the P values (i.e., only the energetics of the process). This hypothesis was tested on the laboratory data, and the b values for $\alpha_{min}$ and $\alpha_{max}$ were found to be nearly equal, as proposed. Other parameters are discussed in later subsections.

A typical example of an f-alpha curve computed from the laboratory data is shown in Figure 3.15. Several features of the curve are to be noted. First, the discontinuity at q = 1 (near the top of the curve) was thought to represent a phase transition, but in fact was apparently a computational deficiency in the method. Second, the curve is smooth because the $D_q$ were developed from curve fits to the results from Equation (3.2). This introduces some computational uncertainties into the resulting f-alpha curve. Third, the curve in Figure 3.15 does not intersect the alpha axis, and must be extrapolated to obtain values of $\alpha_{min}$ and $\alpha_{max}$. This is another source of uncertainty in the results and is discussed below.

Figures 3.16 and 3.17 show the results of computing $\alpha_{max}/\alpha_{min}$ on a typical PNL data file for two values of cell current density, at an ACD (anode to cathode distance) = 3 in., and for two values of the "ripple" imposed on the current to simulate industrial noise. The most noteworthy feature of these curves is the high sensitivity (large slope) at high alumina concentrations, i.e., between 80% and 100% saturations. Although this could provide the needed measure of alumina content, these results were subject to appreciable uncertainties. The computational uncertainties alone were estimated to be ±10%, and the estimated scatter in the data base was ±18%. Uncertainties of this magnitude would normally render the results useless, but the recurring trend (over several data sets) of high slope at high alumina is significant.

These results motivated further analysis of the thermodynamic multifractal method in an attempt to reduce the above uncertainties. It was found that this method inherently loses accuracy with refinements in the box size (b), simply because of the way in which the mathematics are formulated. Another limitation of this method is that it treats only binomial processes, so multinomial processes (such as a distribution of many bath bubble sizes, for example) could not be treated. Also, the computed moments were limited

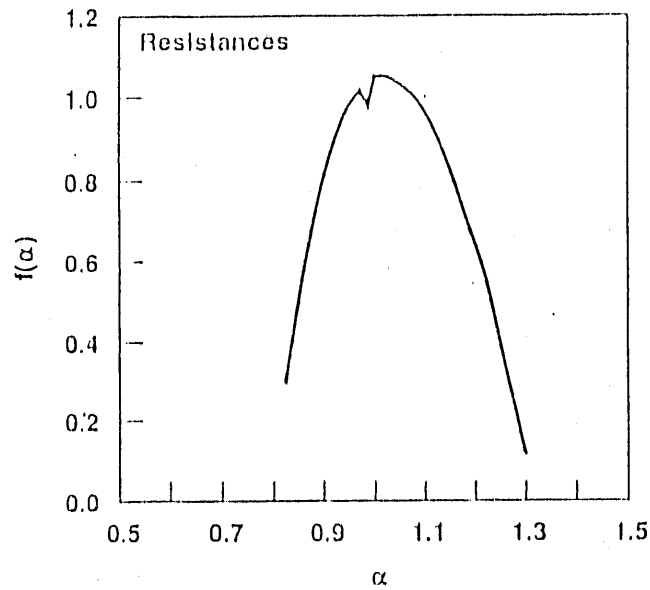


FIGURE 3.15. Typical f-Alpha Curve Obtained from Laboratory Data

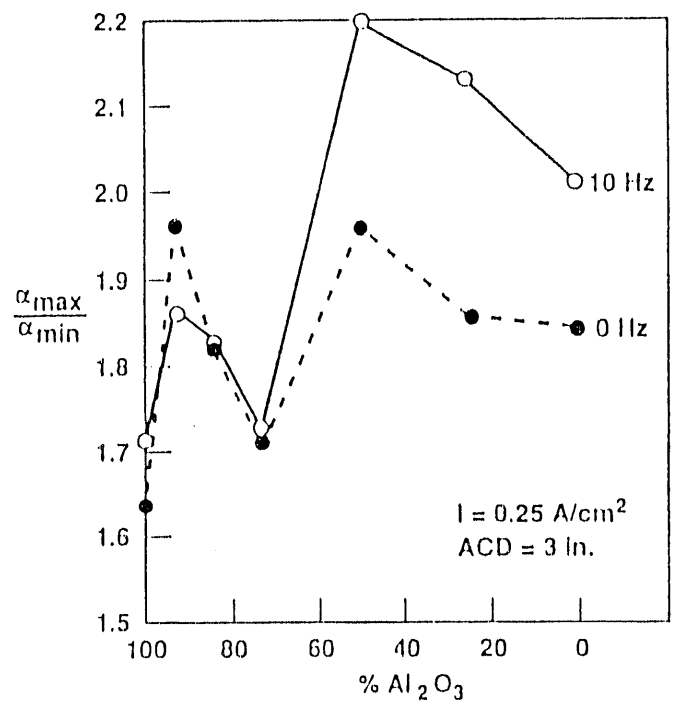


FIGURE 3.16. Variation of the Alpha Ratio Parameter Versus Alumina Concentration (expressed as % saturation) at 0.25 A/cm$^2$

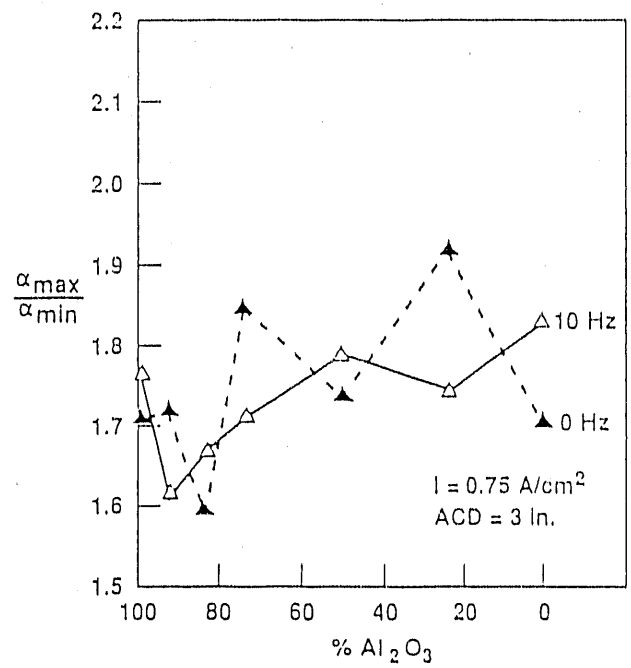


FIGURE 3.17. Variation of the Alpha Ratio Parameter Versus Alumina Concentration (expressed as % saturation) at 0.75 $A/cm^2$

to orders of $-9<q<9$ because of computer precision. Extensions to higher order moments without extrapolation of the f-alpha curve to the alpha axis would require rewriting the computer code in double precision. The resulting computational requirements could eventually impact industrial applications.

In conclusion, the thermodynamic multifractal analysis appeared to give a sensitive and possibly consistent measure of alumina content at high concentrations, but uncertainties in the results were so large that the value of the method in industrial environments was questionable. This deficiency was considered serious enough to lead to a search for an alternative method with better accuracy. Such a method is discussed next.

### 3.3.2 Probabilistic Formalism

PNL staff obtained a preprint of "Probabilistic Multifractals and Negative Dimensions" from A. Chhabra during the August 1990 Gordon Conference on Fractals. This method actually exhibits improved accuracy with refinements in the box size (b), contrary to the results from the thermodynamic approach

described above. It is also able to treat multinomial processes, such as a distribution of bath bubble sizes, which may occur in the system under study.

In the probabilistic formalism, the division of the total normalized signal (resistance integrated over time) into boxes is viewed as cascades of smaller and smaller box sizes considered simultaneously. (This is different from the thermodynamic approach, which considers a single box size at each division.) As each box is divided into smaller and smaller sub-boxes, the ratio between the total signal in successive sets of sub-boxes produces what is known as a multiplier distribution, where the multiplier M has the value $0<M<1$. The number of occurrences of each value of M is used to construct a distribution of the probability, P(M) versus M, as shown in Figure 3.18. A random sample from this P(M) versus M distribution produces the most probable value of M, called M*. Alpha and f are computed as follows:

$$\alpha = -\ln(M*)/\ln(b) \tag{3.6}$$

$$f = D_o + lnP(M*)/\ln(b) \tag{3.7}$$

where $D_o$ is a reference chosen as unity in this work.

These equations arise from the use of the laws of large numbers, but with the following interpretation. Values of f that are negative represent events that occur less than once per box of size b in the data base. Consequently, the very rarest of events in the laboratory cells can be used to extend the f-alpha curves down past the horizontal alpha axis. This widens the f-alpha distribution without the need for extrapolation, and in turn renders the proposed measure of alumina content, $\alpha_{max}/\alpha_{min}$, more sensitive. Also, the accuracy is dependent primarily on the number of samples (N) taken from Figure 3.18, i.e., the error is proportional to $N^{-1/2}$, as in standard Monte Carlo sampling techniques. Computation of moments of order $-20<q<20$ were found to be routine, so there was no need to employ double precision in the computer code.

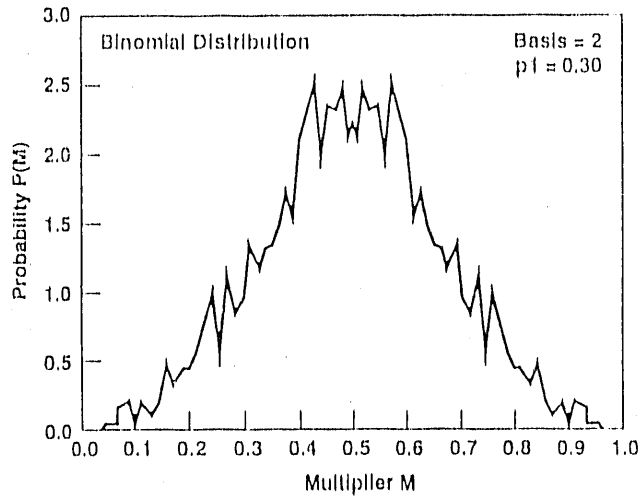


FIGURE 3.18. Multiplier Distribution for 8192 Points

However, this method also has a limitation. The P(M) versus M distribution in Figure 3.18 was generated with 8192 data points from a binomial distribution and is comparable to the experimental data bases of 10,000 data points each. One would expect this to produce a smooth binomial distribution, but it does not. Sampling from Figure 3.18 produces the f-alpha curve shown in Figure 3.19. Although Figure 3.19 is accurate to within ±1.5% (i.e., 4500 samples, as in the laboratory data shown below), the deficiencies of the data are evident in the irregular nature of the f-alpha curve. This was originally thought to be caused by an insufficient number of points in the data base, and was the reason why the pilot cell data were collected in higher density, but for only one anode because of computer memory limitations. However, subsequent analysis has shown that this deficiency was instead due to the lack of "texture" in the data. That is, when an analog signal is converted to a digital signal, there must be enough digital resolution to adequately represent the nonlinear nature of the phenomenon. Insufficient digital resolution means that only a finite number of unique resistance values may occur in a digital record, rather than the infinite number provided by the continuum analog signal. The result is a narrow multiplier distribution, from which it is difficult to sample well enough to produce a smooth f-alpha curve. This is demonstrated further in the following subsections.

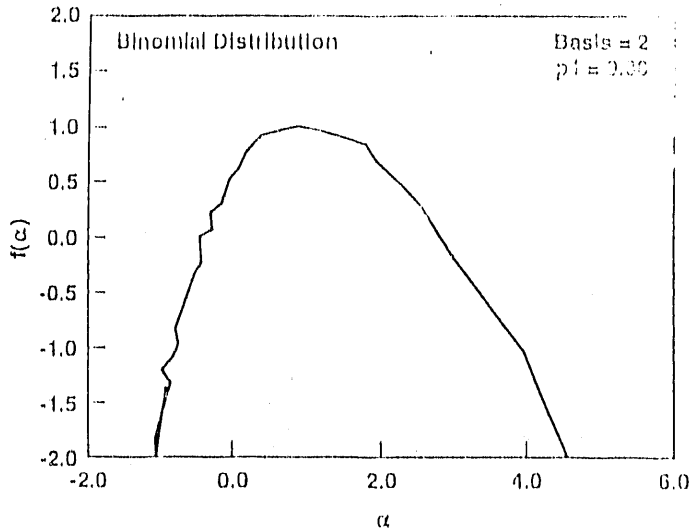


FIGURE 3.19. Binomial f-Alpha Distribution Constructed by Sampling from Figure 3.18

Results for Laboratory Tests

The digital resolution employed to collect the laboratory data was ten divisions of the full-scale signal. A typical multiplier distribution is shown in Figure 3.20, which is more narrow than desired. Such narrow distributions contain fewer data in the tails, and in turn may affect the high order moments in the f-alpha diagram, along with the smoothness of the curve. An example of an f-alpha curve for the laboratory data is shown in Figure 3.21. It exhibits the roughness associated with the finite digital resolution. However, an important objective of using the probabilistic formalism was to eliminate the need to extrapolate the curve to the alpha axis, and Figure 3.21 shows that this was accomplished. In fact, the improved computational accuracy permitted the curve to be computed to f = -2 in order to improve the sensitivity of the $\alpha_{max}$ and $\alpha_{min}$ values. Also note that the postulated phase transition at q = 1 now appears to be of higher order in this particular data set. The reason for this is thought to be due to the improved computational accuracy of the probabilistic multifractal method.

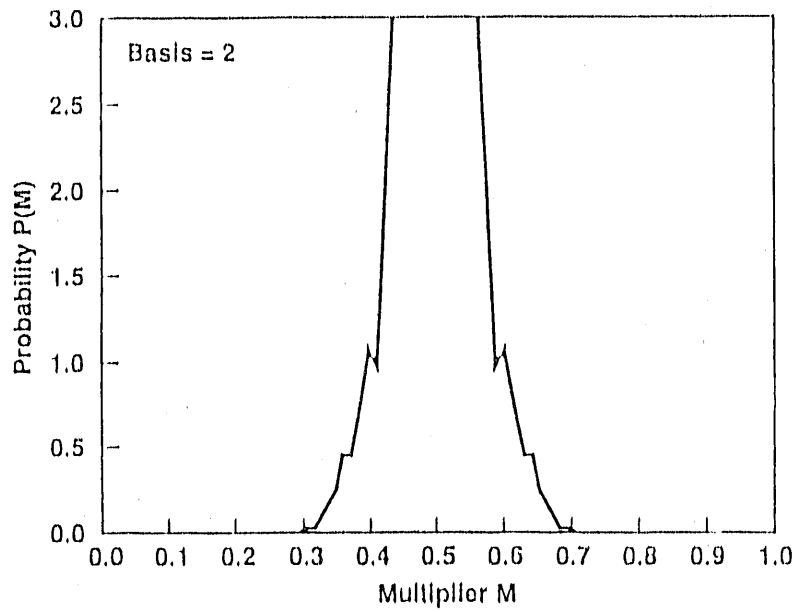


FIGURE 3.20. Typical Multiplier Distribution for Laboratory Data

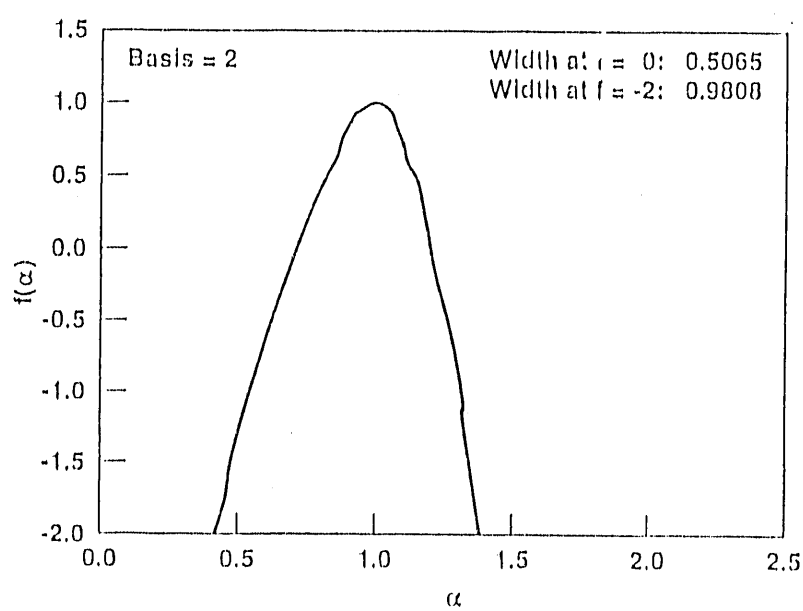


FIGURE 3.21. Typical f-Alpha Curve for Laboratory Data Using a Multiplier Distribution such as that Shown in Figure 3.20

A plot of $\alpha_{max}/\alpha_{min}$ versus alumina concentration obtained using the probabilistic formalism is shown in Figure 3.22. As indicated by the error bars, the computational uncertainties have been reduced by an order of magnitude. The scatter (uncertainty) in the laboratory data base itself was estimated to be ±12% at the 95% confidence level. Unfortunately, this was still comparable to the variations in the alpha ratio versus alumina shown in Figure 3.22. Although the objective of improving computational accuracy was attained, it revealed that the data were too scattered to permit definite conclusions to be reached. However, the sensitivity of the alpha ratio at high alumina concentrations appeared to be retained in the data. This trend encouraged further work using the probabilistic formalism to analyze the pilot cell test data, as described below.

Results for Pilot Cell Test

The current and voltage data for Anode A of the pilot cell test were obtained with a digital resolution of twenty. A series of multiplier distributions and their associated f-alpha diagrams are shown in Figures 3.23 to 3.30. These results are for 85%, 76%, 52%, and 32% saturation of alumina, respectively. There are several things to note from these figures, as follows.

First, the multiplier distribution is wider with the higher digital resolution (twenty) than it was with the lower resolution (ten) used in the laboratory experiments, and the associated f-alpha diagrams are smoother. This is true even for data sets as small as 5000 data points, and suggests that other, lower density data collected during the pilot cell test may also be suitable for chaos theory analysis. The curves in these diagrams also reach f = -2 without the need for extrapolation. It may be concluded that the probabilistic formalism is more sensitive to the "texture" of the data than to the amount of data. The connotation of texture refers to the analog versus digital nature of the data. This means that the method would be relatively fast in an industrial application because fewer data would have to be collected for each cell in the plant. Consequently, the same computer could service more cells in a given time period.

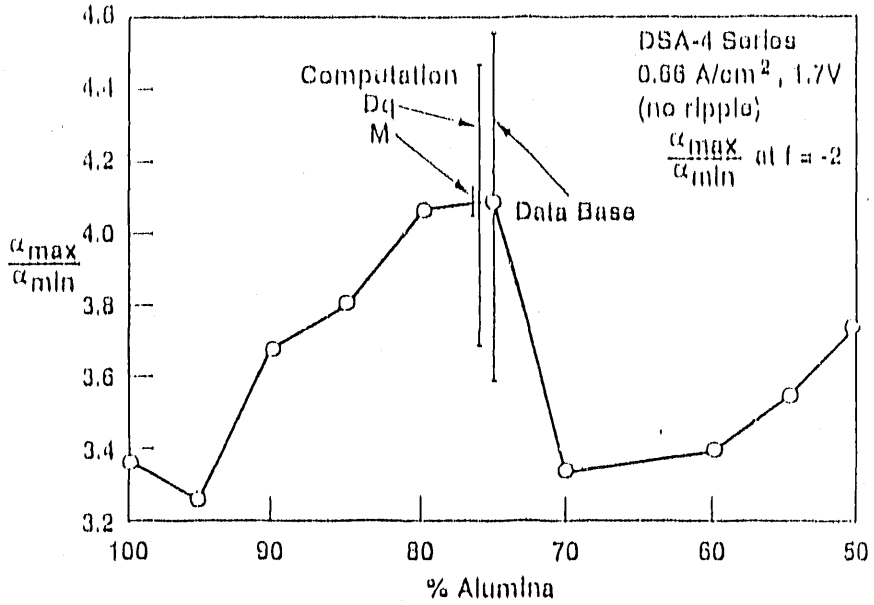


FIGURE 3.22. Typical Results for Alpha Ratio Versus Alumina Concentration for Laboratory Data Using the Probabilistic Multifractal Approach

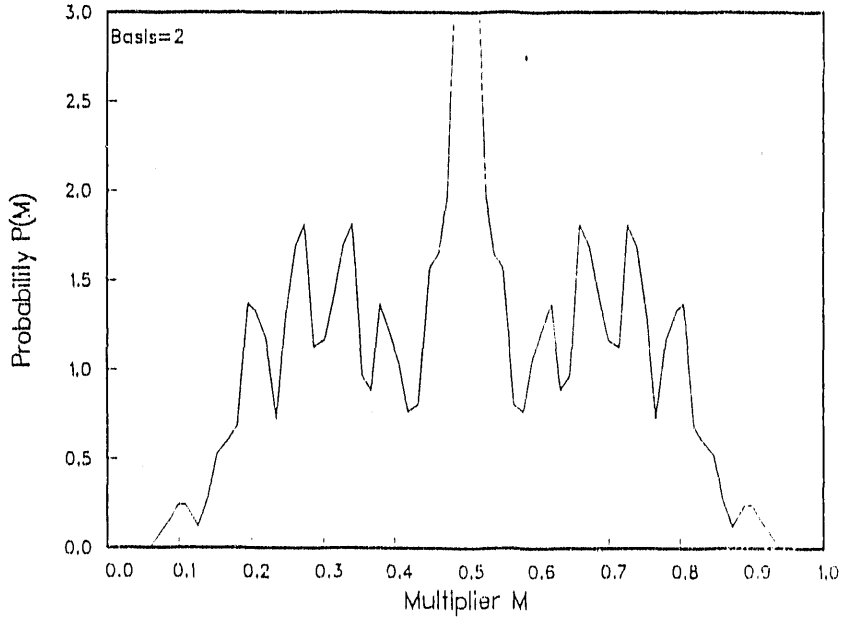


FIGURE 3.23. Multiplier Distribution for File RW4B of the Pilot Cell Test, 85% Alumina

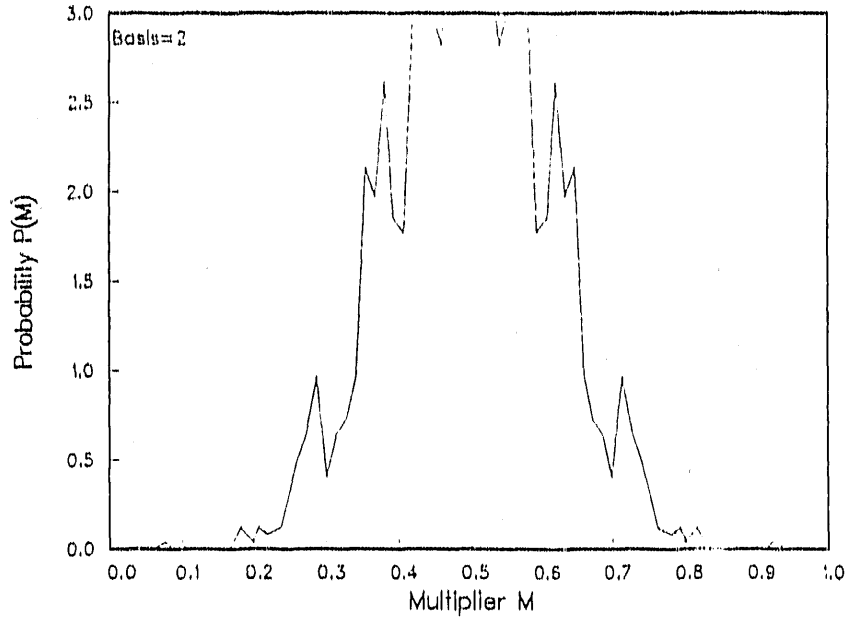


FIGURE 3.24. Multiplier Distribution for File RW1A of the Pilot Cell Test, 76% Alumina

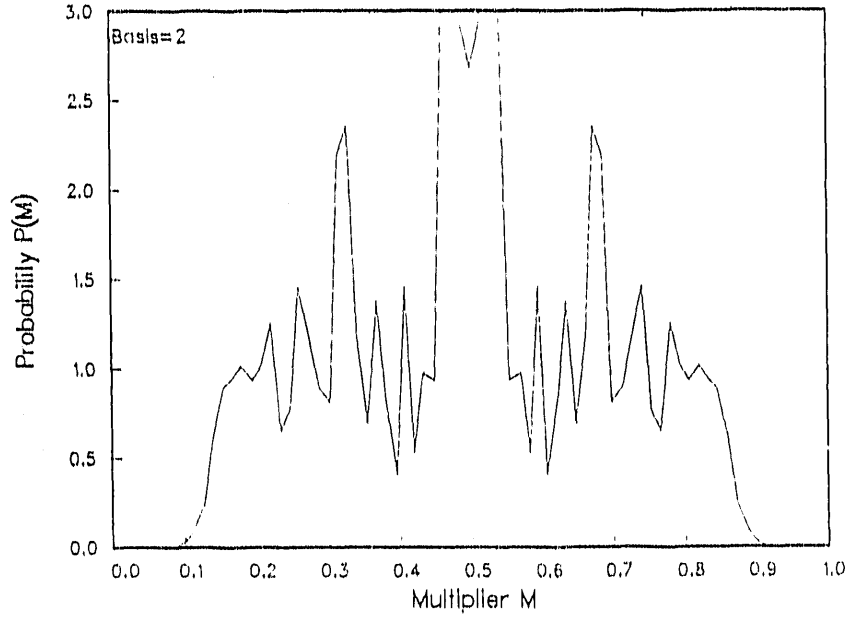


FIGURE 3.25. Multiplier Distribution for File RW22A of the Pilot Cell Test, 52% Alumina

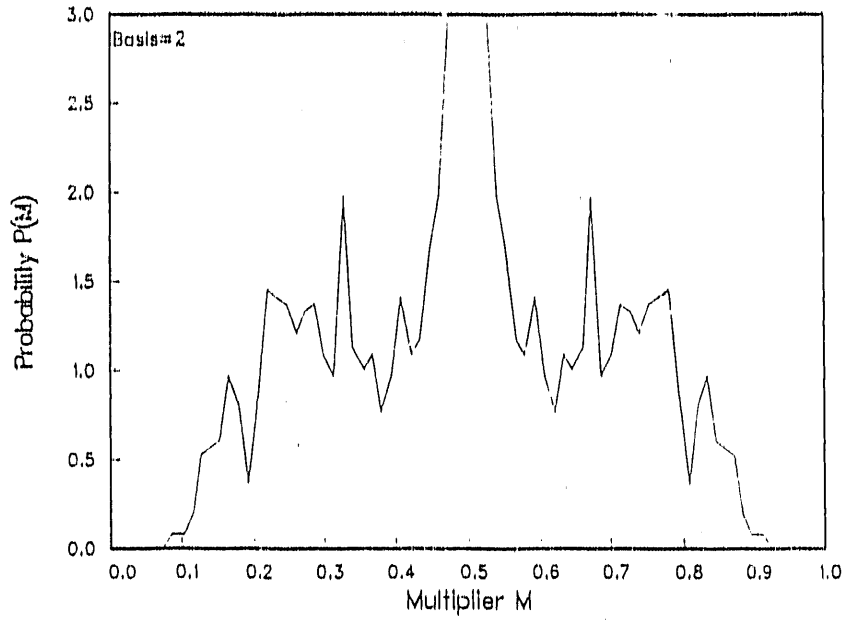


FIGURE 3.26. Multiplier Distribution for File RW29B of the Pilot Cell Test, 32% Alumina

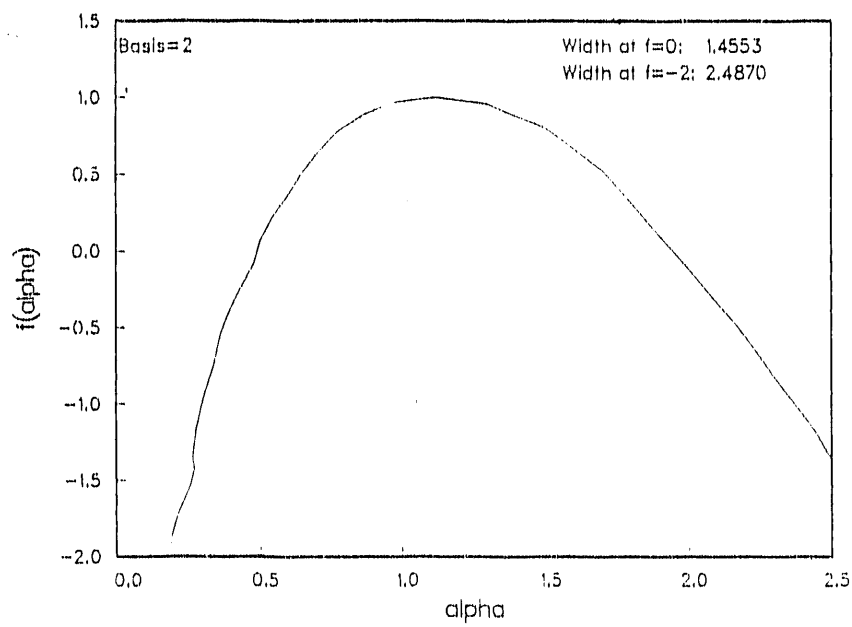


FIGURE 3.27. f-Alpha Distribution for File RW4B of the Pilot Cell Test, 85% Alumina

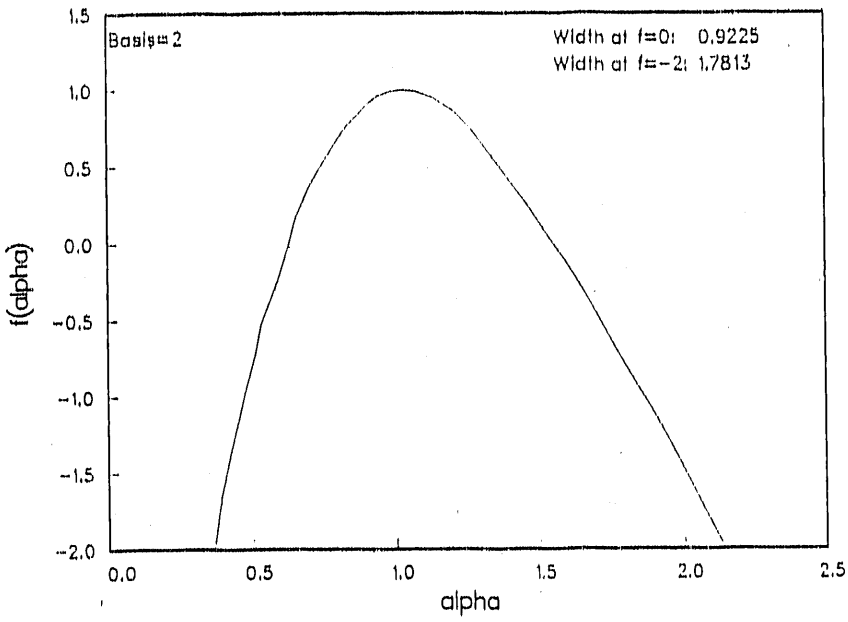


FIGURE 3.28. f-Alpha Distribution for File RW1A of the Pilot Cell Test, 76% Alumina

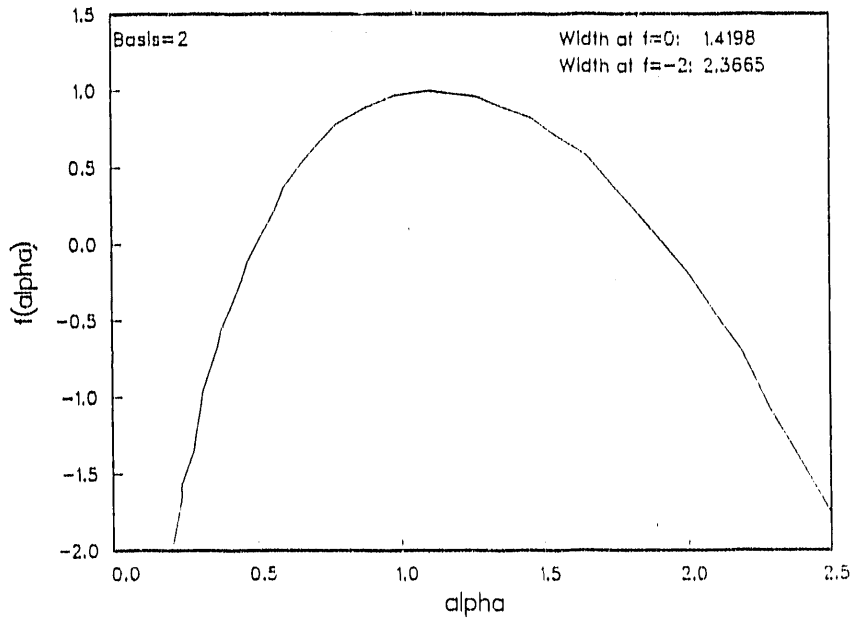


FIGURE 3.29. f-Alpha Distribution for File RW22A of the Pilot Cell Test, 52% Alumina

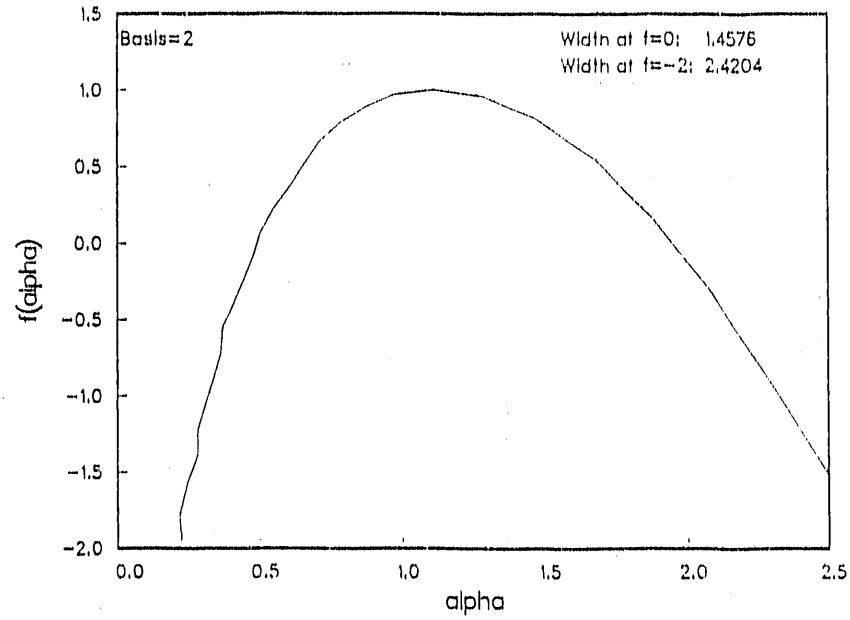


FIGURE 3.30. f-Alpha Distribution for File RW29B of the Pilot Cell Test, 32% Alumina

Second, although the data are of good quality and the method appears to show good sensitivity, there does not appear to be a consistent trend in the alpha ratio versus the alumina content. This can be seen by noting that Figures 3.27, 3.28, 3.29, and 3.30 are only typical examples; other curves show different dependencies on the alumina content. Further clarification is obtained by plotting the alpha ratio as in Figure 3.31. Each data point in Figure 3.31 is the average computed from six files of 10,000 points each (Table 2.1); the vertical bar shows the typical uncertainty at 95% confidence. The solid line in Figure 3.31 is not a curve fit, but is a guide for the eye that indicates the trend in the alpha ratio versus the alumina content. The scatter in Figure 3.31 is comparable in magnitude to the change in mean value, again indicating that the data contain noise factors that are not accounted for in the present analysis. Figure 3.32 shows the alpha ratio versus time for a range of alumina concentrations. Each curve shows results from six consecutive data files collected within 30 min (see Section 2.2). Although the alumina concentration is not expected to change significantly

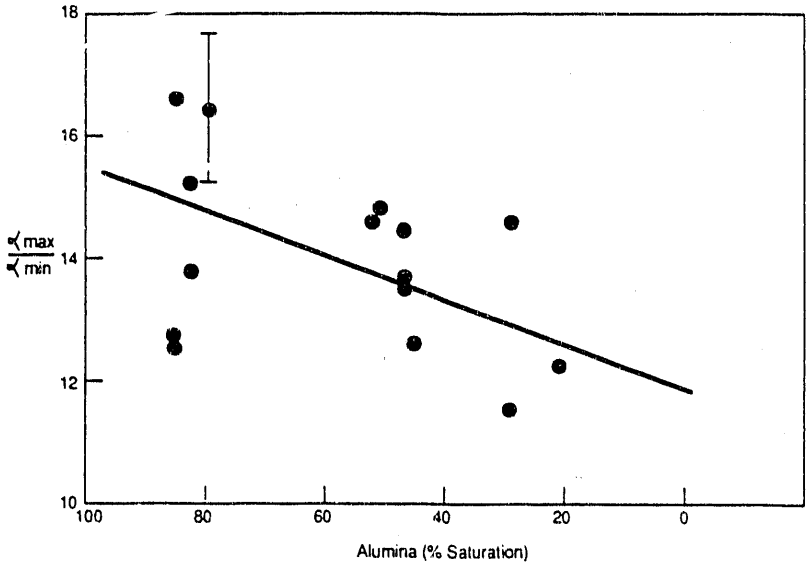


FIGURE 3.31. Alpha Ratios Versus Percent Alumina for Pilot Cell Test

over a period of 30 min, any trend in the curves should be consistently downward) as the alumina is depleted. The curves in Figure 3.32 are thus an indication of the noise in the cell. This is true even when other factors such as the anode current are factored out (see Table 2.1). The above figures are representative of the balance of the data from the pilot cell test: an occasional correlation sometimes appears for certain subsets of data, but by and large the noise dominates and there is no consistency in the trends.

In the interest of thoroughness, nine more combinations of $\alpha_{min}$ and $\alpha_{max}$ were investigated for possible correlations with alumina content. These are described briefly as follows:

- $\alpha_{min}$ versus alumina, because the positive moments had more physical meaning than the negative moments
- $\alpha_{max} - \alpha_{min}$, which is the true width of the f-alpha distribution
- $(\alpha_{max} + \alpha_{min})/2$, which is the average position of the distribution

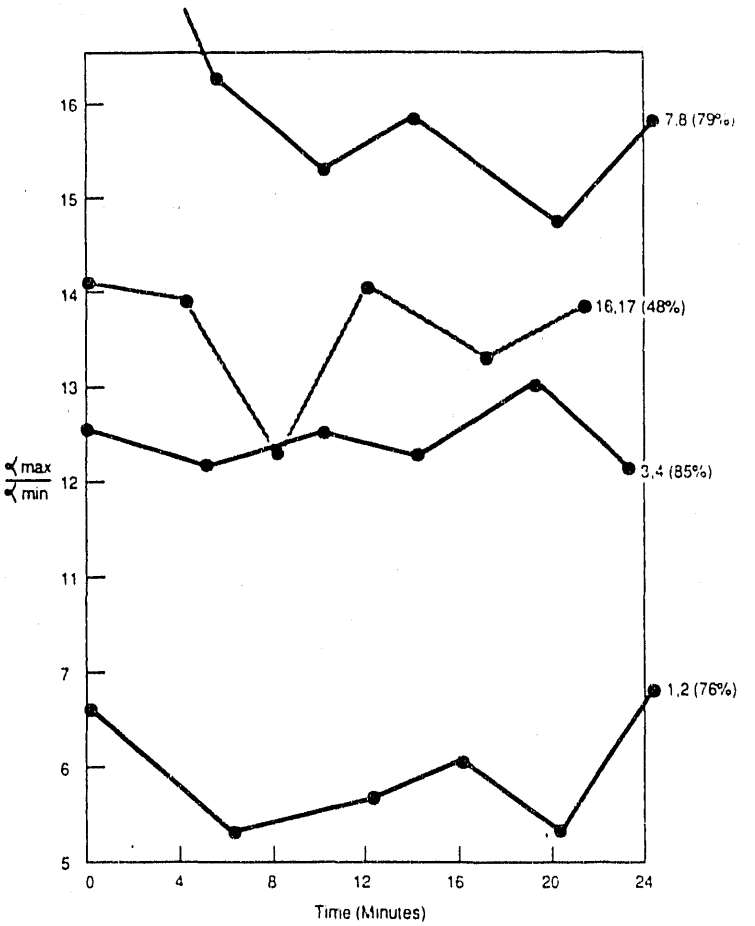


FIGURE 3.32. Alpha Ratios Versus Time for Selected Files from Pilot Cell Test. Notation: 1,2 = file numbers in Table 2.1, 76% = alumina saturation

- the sum of alphas over the difference of alphas, which is analogous to the mathematics of spinodals
- $(\alpha_{max} * \alpha_{min})^{1/2}$, which is the geometric mean
- the sum of alphas times the difference of alphas, supposing that a quadratic form might correlate versus alumina
- the product of the two alphas, for the same reason
- $\alpha_{max}$ versus $\alpha_{min}$, with the alumina concentration as a parameter
- the derivative of the resistances, to amplify changes in the signals.

None of the above attempts gave a successful correlation versus alumina concentration. The results were the same without the voltage correction described in Section 2.2 and with the multinomial rather than binomial assumption. The conclusion was the same as for the alpha ratio: there may be sufficient sensitivity with this method, but consistency is not sufficient to develop a useful correlation versus alumina content from these data.

The most important conclusion that can be reached at this stage of the analysis is that these data do not support the feasibility of using this method to develop a non-intrusive alumina sensor.

## 3.4 OTHER APPROACHES

Three other approaches were briefly explored in an attempt to find some type of correlation between a measured quantity and the alumina concentration. The first of these approaches was a simple Fourier transform with a standard Parzen window, as described in Press et al. (1986). This approach gave the power spectral density of the resistance versus the frequency. A sample of the result is shown in Figure 3.33 for pilot cell test data. Figure 3.33 shows a generally featureless spectrum, rather than a distinct noise tail that could be filtered out. The two apparent small peaks at the mid- and higher-range frequencies are artifacts of a filtering attempt. These spectra do not appear to contain any obviously useful feature other than the DC signal. Thus, the second approach attempted was to try a correlation using resistances computed from the nominal voltages and currents given for each data set in Table 2.1. A null result was again obtained.

The third approach was designed as a test of the basic assumptions employed in this program. It has been assumed in this work that the alumina was uniformly distributed throughout the cell, both in the laboratory experiments and in the pilot cell test. If this is reasonable, then measurement by any single anode would theoretically give the same result as any other anode. However, if this is not true, then different anodes could give different measurements. Furthermore, if the alumina variations are dynamic (i.e., oscillatory or turbulent, rather than a static gradient in the cell), then a single anode may not suffice unless the period of the oscillations are known. It

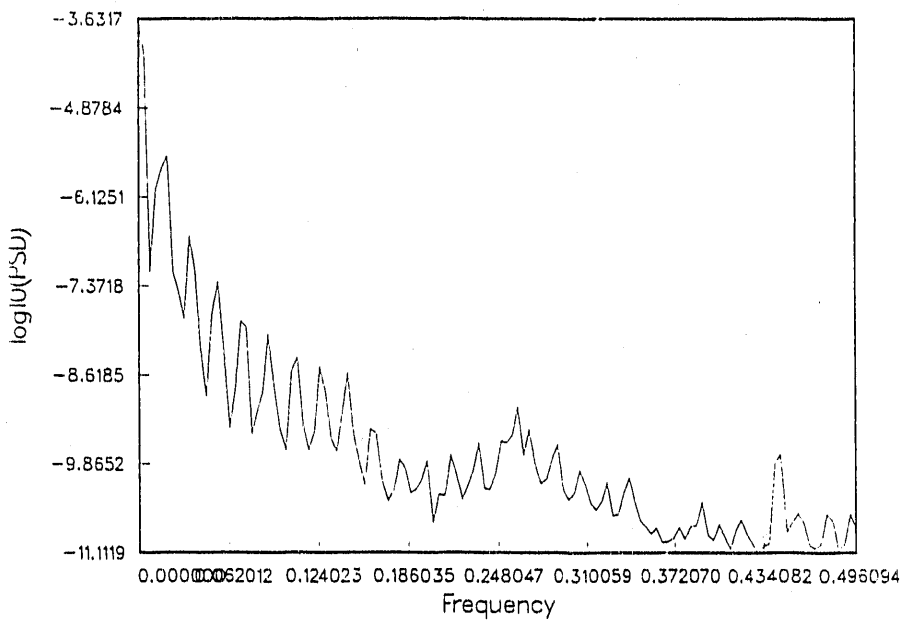


FIGURE 3.33. Typical Power Spectral Density for Pilot Cell Test Data

follows that a more cell-wide characteristic electrical resistance may provide a better correlation. The best approach for this is to simultaneously measure the current for each electrode, and then sum them to obtain the total cell current versus time. This current could then be used with the simultaneously measured cell voltage to compute the cell resistance in a manner quite similar to that for a single anode. Although data of this type were not immediately available for this report, an attempt was made to test the above hypothesis using only the voltage, which was a characteristic of the entire cell. Once again, a null result was obtained. The probabilistic multifractal approach gave adequate sensitivity to an unidentified variable (the noise), but the fluctuations in the alpha ratio could not be correlated versus the alumina concentration.

## 4.0 FEASIBILITY ASSESSMENT

Figure 3.31 is useful in assessing the feasibility of using chaos-based approaches to develop a non-intrusive alumina sensor. The slope of the alpha ratio versus alumina can be estimated at about 0.036/% alumina. The scatter at high alumina concentrations (>80% saturation) can be estimated at ±10% (for each group of six files shown in Table 2.1) to ±25% (for the overall data base in Figure 3.31). Both of these uncertainties are at the 95% confidence level. Multiplying a given alpha ratio (e.g., 15 at 90% alumina) by the uncertainty gives values of 15 * 0.1 = 1.5 to 15 * 0.25 = 3.75. Thus, the signal to noise ratio (for detecting changes in alumina) is about 0.036/1.5 = 0.024 to 0.036/3.75 = 0.009. These are not encouraging numbers. However, if the unidentified noise-producing phenomenon can be understood, uncertainties could conceivably be reduced to the point where they were dominated by the computational uncertainties (±1.5%). If so, the expected error at high alumina concentration would be about 15 * 0.015 = 0.022. This would give a signal to noise ratio of slope/uncertainty = 0.036/0.022 = 1.63, which is more encouraging. The conclusion is that the noise-producing phenomenon must be identified and understood to make further development feasible and possible.

If identification of the noise is considered possible and profitable, the above signal-to-noise ratio can be improved by simply increasing the sampling from the multiplier distribution (see Section 3.3.2). Other computational improvements in accuracy also appear possible.

Several phenomena that could affect the results of signal analyses were mentioned in Section 2. One of these possible noise sources merits discussion here to illustrate the type of effort that must be expended to eventually develop a non-intrusive alumina sensor. This suspected noise source is the large carbon anode that was operated simultaneously with the inert anodes in the pilot cell test. The carbon anode used a separate rectifier. Standard DSA of the pilot cell voltage signals have shown that the DC component of the carbon anode seriously influenced the inert anode signals. It is reasonable to expect that the AC component of the carbon anode had a comparable effect,

except that the time dependence appeared as noise. DSA methods are often suitable for quantifying such effects.

From another perspective, it is also interesting to note that although the laboratory experiments and the pilot cell test were two separate experiments of appreciably different size scales and performed with different facilities, both experiments exhibited noise levels of comparable magnitude. This prompts consideration of features that were common to both experiments. One of these features is described by the following scenario. Both experiments involved bubbling, turbulent baths. It is assumed that the presence of the bubbles affects the resistivity of the bath. The bubble diameters in both experiments were orders of magnitude smaller than the instruments (anodes) used to measure the bath resistivity. It is reasonable to expect that the measurements were actually averages of many smaller ("bubble sized") fluctuations in resistivity. If the micro-scale electrical/bubble processes occurring on the anode surfaces were not uniform (i.e., heterogeneous distributions of resistivity across the diameter of the anodes - 0.5 to 10.0 cm), the heterogeneity could not be measured by an instrument this large in either case. The situation is analogous to measuring turbulence in a wind tunnel: a small anemometer will be much more sensitive than a large windmill.

Recall that the probabilistic multifractal method is essentially a measurement of very rare events. This is true for events of large amplitude ($q>0$) and small amplitude ($q<0$). In either case, a "rare event" means that all phenomena occurring on the anode surfaces are of the same type at the same time. For example, all bubbles simultaneously collapsing or all bubbles simultaneously growing to the same diameter at the same rate. The method seeks out and quantifies both large spikes and periods of quiescence. If such events are indeed sensitive to alumina content, this method should have worked.

There are several possibilities to explain why the probabilistic multifractal method was not successful for these data:

1. Extraneous noise, such as the carbon anode in the pilot cell test, affected the results.

2. The anodes were too large to measure the bath resistance fluctuations at the proper scale (too much averaging).

3. The data were not of sufficient digital resolution to permit mathematical compensation for the anode size, as in the laboratory tests.

4. The alumina-induced bath resistance changes were of much smaller magnitude than the resistance fluctuations induced by the bubbling, turbulence, varying bath ratio, or varying temperature.

5. Measurements using only one anode were not representative of the bath alumina content.

The first three have been discussed above. Industrial practice indicates that the fourth might be true at the higher alumina concentrations. If so, a multivariable statistical analysis may be appropriate. However, assuming for the moment that the bath resistance is sensitive to high alumina concentrations, the fifth item above may present one last opportunity. Two necessary assumptions are that the cell was large enough to permit long-wavelength oscillations in alumina concentration (on the order of the cell diameter), and that the anode/cell diameter ratios were small enough so that the cell fluctuations appeared as noise. What is thus needed is a measure of the resistance for the entire cell, rather than for one location in the cell. For the pilot cell test, this cell-wide measurement can be obtained by adding up the simultaneously measured currents from all the inert anodes. Such a cell-wide measurement of resistance would be consistent with the argument that the alumina content is characteristic of the whole cell. Pilot cell test data that were collected for other signal analysis efforts could be used for this purpose but were not available at the time this report was written.

## 5.0 CONCLUSIONS AND RECOMMENDATIONS

Several conclusions can be reached from this first application of the methods of chaos theory to the analysis of aluminum electrolysis cells, as follows:

- Among the four approaches attempted for data analysis, the first three (phase space plots, Hurst analysis, and thermodynamic multifractals) either gave null results or had insufficient accuracy to produce the needed non-intrusive measurement of alumina concentration.

- The fourth approach (probabilistic multifractals) had sufficient computational accuracy to reveal where improvements could be made in data collection techniques (i.e., greater digital resolution of the analog data). These improvements were implemented in the pilot cell test.

- The probabilistic multifractal approach also showed that the apparent scatter in the results seemed to originate from the data itself, and thus that there was some physical phenomenon that was not properly understood or addressed in the data analysis. The result was that although the computed analysis parameters (e.g., the alpha ratio) exhibited adequate sensitivity to detect variations in this unidentified phenomenon, there was no consistent correlation with the cell alumina concentration. The plotted results had the appearance of noise. This was supported by results from Fourier transform analysis and by the lack of correlation between the nominal DC resistance and the alumina concentration.

- The present data base does not support the use of these chaos-based approaches for developing non-intrusive alumina sensors.

The above conclusions also lead naturally to the following recommendations for further work:

- Analyze the data from all the available anodes in the pilot cell test using chaos approaches, as described in Section 4.0.

- We recommend that industry implement a low-cost "observation post" on any selected cell(s), regardless of anode type, using the phase space plotting method. The phase space method is suggested because of its simplicity and generality. The objective of the observation post is to permit long-term, low-cost collection of data in an effort to find patterns that would be useful for alumina control and for understanding the source of noise. Data collection could be as simple as taking an occasional snapshot of the CRT screen. However, it is important that the responsible process engineer keep a notebook of regular observations so that the trends in the data may be identified over long periods of time. These observations could then be analyzed periodically, perhaps semi-annually, with the hope of finding patterns useful for cell control.

## 6.0 REFERENCES


Frisch, U., and G. Parisi. 1985. "On the Singularity Structure of Fully Developed Turbulence." Turbulence and Predictability in Geophysical Fluid Dynamics, ed. M. Ghil, North-Holland, New York, p. 84.

Halsey, T. C., M. H. Jensen, L. P. Kadanoff, I. Procaccia, and B. I. Shraiman. 1986. "Fractal Measures and Their Singularities: The Characterization of Strange Sets." Physical Rev. A, Vol. 33, No. 2, p. 1141.

Hart, P. E., B. B. Brenden, N. C. Davis, O. H. Koski, S. C. Marschman, K. H. Pool, C. H. Schilling, C. F. Windisch, and B. J. Wrona. 1987. Inert Anode/Cathode Program: Fiscal Year 1986 Annual Report." PNL-6247, Pacific Northwest Laboratory, Richland, Washington.

Hurst, H. E. 1951. "Long Term Storage Capacity of Reservoirs," Trans. Am. Soc. Civil Engr., Vol. 116, p. 770.

Meneveau, C., and K. R. Sreenivasan. 1987. Nuclear Physics B, Vol. 2, Supplement, p. 49.

McQuarrie, D. A. 1973. Statistical Mechanics, Harper and Rowe, New York.

Press, W. H., B. P. Flannery, S. A. Teulolsky, and W. T. Vetterling. 1986. Numerical Recipes, Cambridge University Press, New York.

Skybakmoen, E., A. Solkeim, and A. Sterten. 1990. Light Metals 1990, The Minerals and Materials Society (TMS), Warrendale, Pennsylvania, pp. 317-324.

Williford, R. E. 1988. "Multifractal Fracture," Scripta Metallurgica et Materialia, Vol. 22, p. 1749.

Windisch, Jr., C. F., T. R. Alcorn, and A. T. Tabereaux. 1991. Test Plan for the Pilot Cell Test of Inert Anodes: Report on the June 1991 Meeting at the Reynolds Metals Company Facility. PNL-7802, Pacific Northwest Laboratory, Richland, Washington.

Windisch, Jr., C. F., O. H. Koski, N. D. Stice, C. L. Nikias, and L. G. Morgan. 1990. Fiscal Year 1989 Annual Report for the Sensors Development Program. PNL-7309, Pacific Northwest Laboratory, Richland, Washington.

# DISTRIBUTION

No. of
Copies

OFFSITE

M. J. McMonigle
U.S. Department of Energy
Office of Industrial Programs
Forrestal Building
Washington, DC 20585

P. H. Salmon-Cox
U.S. Department of Energy
Office of Industrial Programs
Forrestal Building
Washington, DC 20585

12 DOE Office of Scientific and Technical Information

Dr. T. Alcorn
Manufacturing Technology Laboratory
Reynolds Metals Co.
3326 East 2nd Street
Muscle Shoals, AL 35661-1258

C. Anderson
Columbia Aluminum Co.
85 John Day Dam Road
Goldendale, WA 98620

J. V. Anderson
WCVE3
EG&G Idaho, Inc.
Idaho Falls, ID 83415

D. Auburg
Bonneville Power Administration
P.O. Box 3621, PDX 97208
Portland, OR 97208

F. W. Baker
Ceramics Division
Alcoa Laboratories
Alcoa Center, PA 15069

No. of
Copies

M. Baltzell
Eastalco Aluminum Company
Alumax, Inc.
5601 Manor Woods
Frederick, MD 21701

J. A. Barclay
U.S. Bureau of Mines
2401 "E" Street N.W.
Washington, DC 20241

H. Robert Baumgartner
Ceramics Division
Alcoa Laboratories
Alcoa Center, PA 15069

T. R. Beck
Electrochemical Technology Corp.
1601 Dexter Avenue
Seattle, WA 98109

S. Berwagan
Bonneville Power Administration
P.O. Box 3621 K
Portland, OR 97208

T. M. Besmann
Metals and Ceramics Division
Oak Ridge National Laboratory
P.O. Box X, Bldg. 4515
Oak Ridge, TN 37831-6063

K. A. Blakely
President
Advanced Refractory Technologies, Inc.
699 Hertel Ave.
Buffalo, NY 14207

M. H. Blenk
Du Pont
P.O. Box 787
Niagara Falls, NY 14302

No. of
Copies

L. G. Boxall
Martin Marietta Laboratories
1450 South Rolling
Baltimore, MD 21227

J. Bracher
Kaiser Aluminum and Chemical
Corp.
825 N.E. Multnomah St.,
Suite 960
Portland, OR 97232-2150

R. Brandt
Department of Materials
Science and Engineering
University of Washington FB-10
Seattle, WA 98195

J. J. Brown, Jr.
Materials Engineering
Virginia Polytechnic Institute
Blacksburg, VA 24061

A. Budner
Bonneville Power Administration
P.O. Box 3621--EPA
Portland, OR 97208

A. J. Caputo
Development Division
Oak Ridge Y-12 Plant
Building 9202 MS-8095
Oak Ridge, TN 37831-8095

N. Clark
Bonneville Power Administration
Industrial Conservation
P.O. Box 3621
Portland, OR 97208

A. Cooke
Martin Marietta Laboratories
1450 South Rolling
Baltimore, MD 21227

No. of
Copies

J. A. Coppola
Standard Oil Engineered
Materials Company
P.O. Box 156
Niagara Falls, NY 14302

R. Curtis
Materials Development
Corporation
81 Hicks Avenue
Medford, MA 02155

J. V. Day
Kaiser Aluminum and Chemical
Corp.
E 2111 Hawthorne Road
Mead, WA 99021

D. H. DeYoung
Alcoa Technical Center
Alcoa Center, PA 15069

S. Diamond
Battelle Columbus Laboratories
505 King Avenue
Columbus, OH 43201-2693

T. Dwonch
Snake River District BPA
101 W. Poplar
Walla Walla, WA 99362

G. L. Eitel
Stone & Webster Engineering Corp
Greenwood Plaza Box 5406
Denver, CO 80217

R. Engdahl
Deposits and Composites, Inc.
318 Victory Drive
Herndon, VA 22070

No. of
Copies

J. F. Elliott
MIT
Room 4-138
77 Massachusetts Avenue
Cambridge, MA 02139

B. G. Epstein
A. D. Little, Inc.
955 Lenfant Plaza SW 4200
Washington, DC 20024-2119

J. W. Evans
University of California
Dept of Matl. Sci. and Mineral Eng.
Berkeley, CA 94720

R. A. Fenimore
ICI Advanced Materials
Rollins Building, Eighth Floor
Wilmington, DE 19897

D. A. Figgins
ARCO Petroleum Products Co.
P.O. Box 61004
Anaheim, CA 92803-6104

P. Foster
Alcoa Laboratories
P.O. Box 772
New Kensington, PA 15068

J. Gee
Great Lakes Research Corp
P.O. Box 1031
Elizabethton, TN 37643

T. Gilligan
Eltech Systems Corp.
625 East Street
Fairport Harbor, OH 44077

W. M. Goldberger
Superior Graphite Co.
120 S. Riverside Plaza
Chicago, IL 60606

No. of
Copies

J. Goodwell
Center for Metals Production
Mellon Institute
4400 Fifth Avenue
Pittsburgh, PA 15213

Dr. Janet Gregg
Eltech Research Corporation
625 East Street
Fairport Harbor, OH 44077

J. A. S. Green
Martin Marietta Laboratories
1450 South Rolling
Baltimore, MD 21227

C. Griffin
Ceramatec Inc.
2425 S. 900 West
Salt Lake City, UT 84119

L. I. Grindstaff
Great Lakes Research Corp.
P.O. Box 1031
Elizabethton, TN 37643

J. Haggerty
MIT
Building 12, Room 009
77 Massachusetts Avenue
Cambridge, MA 02139

I. L. Harry
Electric Power Research Institute
P.O. Box 10412
Palo Alto, CA 94303

W. E. Haupin
2820 7th Street Road
Lower Burrell, PA 15068

R. Hill
Union Carbide Corp.
P.O. Box 94637
Cleveland, OH 44101

No. of
Copies

H. F. Hillegass
Alcoa Wenatchee Works
P.O. Box 221
Wenatchee, WA 98807

D. G. Howitt
College of Engineering
University of California, Davis
Davis, CA 95616

F. R. Huettig
Advanced Magnetics, Inc.
45 Corey Lane
Medham, NJ 07945

G. R. Hyde
U.S. Bureau of Mines
2401 "E" Street N.W.
Washington, DC 20241

S. C. Jacobs
Primary Processing
Aluminum Company of America
Alcoa Technical Center
Alcoa Center, PA 15069

S. H. Jan
Tennessee Valley Authority
R&D Division - MR 3A
Chattanooga, TN 37401

N. Jarrett
149 Jefferson Avenue
New Kinsington, PA 15068

J. Johnson
Intalco Aluminum Company
P.O. Box 937
Ferndale, WA 98248

L. Joo
Great Lakes Research Corp.
P.O. Box 1031
Elizabethton, TN 37643

No. of
Copies

M. Karmous
Oregon State Department of
Energy
625 Marion Street, N.E.
Salem, OR 97310

R. Keller
RD 3 Roundtop Road
Export, PA 15632

C. W. Koerr
The Stackpole Corporation
Cermag Division
201 Stackpole Street
St. Marys, PA 15847

K. Krupinski
Aristech Research
1000 Tech Center Dr.
Monroeville, PA 15146

G. Y. Lai
Cabot Corporation
P.O. Box 9013
Kokomo, IN 46902-9013

R. A. Landy
Director of Research
North American Refractories Co.
3127 Research Dr.
State College, PA 16801

J. E. Lane
Ceramic Research and
Development Center
Westinghouse Electric Corp.
1310 Beulah Road
Pittsburgh, PA 15235

Sai-Kwing Lau
Standard Oil Engineered
Materials Company
Niagara Falls R&D Center
P.O. Box 832
Niagara Falls, NY 14302

No. of
Copies

J. J. Leddy
Dow Chemical U.S.A.
1776 Building
Midland, MI 48640

W. W. Liang
Gas Research Institute
8600 West Bryne Mawr Avenue
Chicago, IL 60631

W. H. Link
Columbia Aluminum Corp.
85 John Day Dam Road
Goldendale, WA 98620

S. Loftness
Washington State Energy Office
400 E. Union
Olympia, WA 98504

W. Long
Building B815
Dow Chemical
Freeport, TX 77541

A. G. Longmuir
Kaiser Aluminum and Chemical
Corp.
P.O. Box 877
Pleasanton, CA 94566

R. A. Lowden
Metals and Ceramics Division
Oak Ridge National Laboratory
P.O. Box X, Bldg, 4515
Oak Ridge, TN 37831-6063

W. N. Maclay
Koppers Company, Inc.
1005 William Pitt Way
Pittsburgh, PA 15238-1336

J. C. McCloskey
Ten Mile River Associates
296 Mt. Hope Street
North Attleboro, MA 02760

No. of
Copies

Prof. G. Mamantov
University of Tennessee
Knoxville, TN 97996

S. C. Manaktala
Manager of Technology
Reduction Division
Kaiser Aluminum and Chemical
Corp.
300 Lakeside Drive
Oakland, CA 94643

V. H. Markant
Du Pont
P.O. Box 787
Niagara Falls, NY 14302

C. J. McMinn
Manufacturing Technology
Laboratory
Reynolds Metals Co.
3326 East 2nd Street
Muscle Shoals, AL 35661-1258

C. H. McMurtry
Standard Oil Engineered
Materials Company
Niagara Falls R&D Center
P.O. Box 832
Niagara Falls, NY 14302

M. A. Mitnick
Avco Specialty Materials
Subsidiary of Textron Inc.
2 Industrial Avenue
Lowell, MA 01851

H. Mortensen
R. Palika
Cercom, Inc.
P.O. Box 70
Vista, CA 92083

P. Ness
Washington State Dept of Trade
and Economic Development
2001 6th Avenue #2600
Seattle, WA 98121-2522

No. of
Copies

J. R. Payne
Kaiser Aluminum and Chemical
Corp.
P.O. Box 877
Pleasanton, CA 94566

T. Payne
Columbia Falls Aluminum Co.
Columbia Falls, MT

W. Pebley
Oregon Freeze Dry Corp.
525 25th Avenue SW
P.O. Box 1048
Albany, OR 97321

R. D. Peterson
Manufacturing Technology
Laboratory
Reynolds Metals Co.
3326 East 2nd Street
Muscle Shoals, AL 35661-1258

T. R. Pritchett
Kaiser Aluminum and Chemical
Corp.
P.O. Box 877
Pleasanton, CA 94566

W. W. Pritsky
Aluminum Association
900 19th St. N.W.
Washington, DC 20006

S. P. Ray
Alcoa Technical Center
Alcoa Center, PA 15069

Resource Center
Washington State Dept of Trade
and Economic Development
2001 6th Avenue #2700
Seattle, WA 98121-2522

No. of
Copies

J. F. Rhodes
Advanced Composite Materials
Corp.
1525 S. Buncomb Rd.
Greer, SC 29651

N. E. Richards
Manufacturing Technology
Laboratory
Reynolds Metals Co.
3326 East 2nd Street
Muscle Shoals, AL 35661-1258

J. J. Ritter
Ceramics Division
National Bureau of Standards
Gaithersburg, MD 20899

R. C. Rohwedder
3028 Ohio Street Longview, WAD.
R. Sadoway MIT Room 8-109
77 Massachusetts Avenue
Cambridge, MA 02139

W. Scott
Department of Materials
Science & Engineering
Wilcox Hall FB-10
University of Washington
Seattle, WA 98195

D. R. Secrist
Great Lakes Research Corp.
P.O. Box 1031
Elizabethton, TN 37643

A. B. Shah
Noranda Aluminum, Inc.
P.O. Box 70
New Madras, MO 36869

N. Shelton
Intalco
1300 S.W. 5th, Suite 3508
Portland, OR 97201

No. of
Copies

Brian Spector
Pace Consultants
4848 Loop Central Drive
Houston, TX 77081

F. W. Spillers
Dow Chemical U.S.A.
B-1210 Building
Freeport, TX 77541

Dr. Richard M. Spriggs
Office of the Director
Center for Advanced
Ceramic Technology
Alfred University
Alfred, NY 14802

D. V. Stewart
Manufacturing Technology
Laboratory
Reynolds Metals Co.
3326 East 2nd St.
Muscle Shoals, AL 35661-1258

D. Strahan
Reynolds Metals Company
P.O. Box 27003
Richmond, VA 23261

A. T. Tabereaux
Manufacturing Technology
Laboratory
Reynolds Metals Co.
3326 East 2nd Street
Muscle Shoals, AL 35661-1258

G. P. Tarcy
Aluminum Company of America
Alcoa Technical Center
Alcoa Center, PA 15069

P. Thaure
Alumax, Inc.
5655 Peachtree Parkway
Norcross, GA 30092

No. of
Copies

W. H. Thielbahr
Conservative Technology
Division
DOE-Idaho Operations Office
785 DOE Place
Idaho Falls, ID 83402

S. Thomson
General Manager
Klickitat PUD
1313 S. Columbus
Goldendale, WA 98620

R. Unger
Merner Research
P.O. Box 248
Ridgewood, NJ 07451

A. Vinnard
Bonneville Power
Administration (KWI)
P.O. Box 3621
Portland, OR 97208

T. Von Muller-KWI
Bonneville Power Administration
P.O. Box 3621
Portland, OR 97208

D. H. Weinblatt
AIMCOR
One Parkway North
Deerfield, IL 60015

J. D. Weyand
EG&G Idaho, Inc.
Idaho Falls, ID 83415

B. Wilcox
Northwest Aluminum Co.
3313 W. Second St.
The Dalles, OR 97058

C. B. Wilson
Dow Chemical U.S.A.
Texas Operations
B-101 Building
Freeport, TX 77541

No. of
Copies

J. C. Withers
Keramont Research Corporation
4233 S. Fremont Avenue
Tucson, AZ 85714

FOREIGN

D. Brodie
Comalco Ltd.
55 Collins St.
Melbourne,
AUSTRALIA

H. Connor
Group Licensing Controller
Johnson Matthey, plc
New Garden House
78 Hatton Garden
London EC1N 8JP
ENGLAND

T. Kjar
Comalco Ltd.
55 Collins St.
Melbourne,
AUSTRALIA

E. W. Dewing
Alcan International
P.O. Box 8400
Kingston, Ontario
CANADA K7L 4Z4

D. N. MacMillan
Alcan International
C.P. 1250
Jonquieve, Quebec
CANADA G7S 4K8

A. Oye
Institute of Inorganic
Chemistry
Norwegian Institute of
Technology
University of Trondheim
N-7034 Trondheim-NTH,
NORWAY

No. of
Copies

J. Thonstad
Laboratories of Industrial
Electrochemistry
Norwegian Institute of
Technology
University of Trondheim
N-7034 Trondheim-NTH,
NORWAY

K. O. Vee
ASV Ardal Verk
N-5875 Ardalstargen,
NORWAY

Dr. Eric Frazer
CSIRO Australia
Division of Mineral Products
339 Williamstown Road
P.O. Box 124
Port Melbourne, Vic 3207

ONSITE

DOE Richland Field Office

D. R. Segna

28 Pacific Northwest Laboratory

M. Clement
D. K. Hilliard
G. L. McVay
N. L. Moore
L. G. Morgan
D. M. Strachan
R. W. Westerman
R. E. Williford (5)
C. F. Windisch (10)
Publishing Coordination
Technical Report Files (5)

# END

# DATE FILMED

5/8/92